

# Effects of Precursor Composition on the Local Structure of Cu Dispersed on Mesoporous Silica: A Detailed X-ray Absorption Spectroscopy Study

Ian J. Drake,<sup>†</sup> Kyle L. Fajdala,<sup>‡,§</sup> Sal Baxamusa,<sup>†</sup> Alexis T. Bell,<sup>\*,†,§</sup> and T. Don Tilley<sup>‡,§</sup>

Department of Chemical Engineering, University of California—Berkeley, Berkeley, California 94720-1462,

Department of Chemistry, University of California—Berkeley, Berkeley, California 94720-1461, and Chemical Sciences Division, Lawrence Berkeley National Laboratory, 1 Cyclotron Road, Berkeley, California 94720

Received: March 31, 2004

A low-temperature grafting approach using two Cu<sup>I</sup> molecular precursors ([CuOSi(O'Bu)<sub>3</sub>]<sub>4</sub> and [CuO'Bu]<sub>4</sub>) and a high-temperature exchange reaction using CuCl were utilized with a mesoporous silica support (SBA-15) to investigate the effects of catalyst preparation on the nature of copper–support interactions and site speciation. Detailed X-ray absorption near-edge spectroscopy (XANES) and extended X-ray absorption fine-structure studies (EXAFS) studies were performed to characterize the nature of the Cu sites and the Cu–support interactions. The freshly prepared materials from the nonaqueous grafting of [CuOSi(O'Bu)<sub>3</sub>]<sub>4</sub> (CuOSi/SBA (*x.x*), where *x.x* refers to the Cu weight %) exhibit Cu<sup>I</sup> site isolation (by EXAFS and XANES). In contrast, EXAFS and XANES studies of the freshly prepared materials from the nonaqueous grafting of [CuO'Bu]<sub>4</sub> (CuO'Bu/SBA (*x.x*)) suggest that the Cu–O–Cu linkages of the molecular precursor remain intact upon interacting with the support. Isolated Cu<sup>I</sup> sites are observed as the major species in the freshly prepared material from the high-temperature exchange reaction using CuCl (CuCl/SBA (3.0)) (by XANES and EXAFS). Treatment of the materials under He at 573 K leads to loss of the organic species from the grafted materials (by <sup>1</sup>H NMR spectroscopy, thermogravimetric analysis, EA, and IR spectroscopy). EXAFS and XANES studies revealed that CuCl/SBA (3.0) and the CuOSi/SBA (*x.x*) materials still exhibit up to 95% isolated Cu<sup>I</sup> sites, whereas the CuO'Bu/SBA (*x.x*) materials only exhibit Cu as Cu<sup>0</sup> nanoparticles of ca. 7 Å in diameter. After calcination under O<sub>2</sub> at 573 K, residual chloride from the high-temperature preparation of CuCl/SBA (3.0) leads to formation of crystalline CuO particles, whereas the CuOSi/SBA (*x.x*) and CuO'Bu/SBA (*x.x*) materials exhibit more amorphous CuO character after an identical oxidative treatment.

## Introduction

Supported Cu catalysts are known to be active for a variety of reactions, including methanol synthesis,<sup>1</sup> methanol partial oxidation,<sup>2</sup> oxidative carbonylation of methanol,<sup>3</sup> and NO reduction.<sup>4</sup> In most cases, such catalysts are produced by incipient wetness impregnation, ion exchange, or deposition–precipitation.<sup>1–4</sup> The support is then dried, and the deposited copper precursor is calcined in air or oxygen to produce small particles of copper oxide. Reduction of the dispersed metal oxide produces crystallites of Cu with an average diameter of typically 30–110 Å (see for example ref 5). Achieving particle diameters of less than 10 Å is difficult, because Cu readily agglomerates at high temperatures during both the calcination and reduction phases of catalyst preparation.<sup>6</sup> Preparation of very highly dispersed Cu catalysts would be of interest for several reasons. First, it is known that in the size range of ~2 to 10 Å the properties of Cu, and in fact all metals, are intermediate between those of individual metal atoms or cations and bulk metal.<sup>7</sup> The consequences of this for catalysis are illustrated by our recent studies of dimethyl carbonate (DMC) synthesis via oxidative carbonylation of methanol, which show that both the turnover frequency and the selectivity for DMC depend on the dispersion

of Cu. A high turnover frequency and high selectivities to DMC relative to both methanol and CO are achieved for nearly atomically dispersed Cu relative to what is obtained with catalysts containing poorly dispersed Cu.<sup>8</sup> A second motivation for preparing highly dispersed Cu is to use such a material to produce supported Cu catalysts with a chosen average Cu particle size by controlled sintering of the dispersed Cu.

A number of investigations have shown that high dispersions of metal atoms can be achieved using metal-containing molecular precursors introduced onto the support by either chemical vapor deposition or grafting.<sup>9</sup> In the first cases, the precursor is often a metal salt, which can be sublimed, whereas in the second case the precursor is an organometallic compound, which is soluble in a nonaqueous solvent. In both methods of catalyst preparation, the precursor reacts with hydroxyl groups present on the support surface to produce atomically dispersed species. The initially deposited form of the metal can then be oxidized or reduced, depending on the ultimate use of the catalyst. Molecular precursors of the type described have been used successfully to prepare atomically dispersed Ti,<sup>10</sup> Ta,<sup>11</sup> Hf,<sup>11</sup> Al,<sup>11</sup> W,<sup>11</sup> Cr,<sup>11</sup> Fe,<sup>12</sup> Rh,<sup>13</sup> and Pd.<sup>13</sup> The local environment of the dispersed metal in such catalysts can be established from extended X-ray absorption fine-structure (EXAFS) measurements, which can provide information about the nature and coordination of atoms in the first, second, and sometimes third shell of atoms surrounding the atom of interest.<sup>14</sup>

The work presented here addresses the effects of precursor composition on the dispersion of Cu on mesoporous silica (SBA-

\* To whom correspondence should be addressed. Phone: 510-642-1536. Fax: 510-642-4778. E-mail: bell@cchem.berkeley.edu.

<sup>†</sup> Department of Chemical Engineering, University of California—Berkeley.

<sup>‡</sup> Department of Chemistry, University of California—Berkeley.

<sup>§</sup> Chemical Sciences Division, Lawrence Berkeley National Laboratory.

15).<sup>15</sup> Materials were prepared via a low-temperature grafting of molecular precursors  $[\text{CuOSi}(\text{O}^t\text{Bu})_3]_4$ <sup>16</sup> and  $[\text{CuO}^t\text{Bu}]_4$ <sup>17</sup> and by a high-temperature reaction of CuCl with the silanol groups present on the support surface. The local environment of Cu in each sample was characterized by X-ray absorption near-edge structure (XANES) and EXAFS spectroscopies, after initial deposition of Cu and following thermal treatments in He and O<sub>2</sub>. Analyses of EXAFS data were carried out using information obtained from a series of well-defined standards. A preliminary communication describing the interactions of  $[\text{CuSi}(\text{O}^t\text{Bu})_3]_4$  has been reported.<sup>18</sup>

## Experimental Section

**General.** All synthetic manipulations were performed under an inert atmosphere (N<sub>2</sub>) using standard Schlenk techniques or a Vacuum Atmospheres drybox, unless noted otherwise. All dry solvents used were distilled from sodium/benzophenone, potassium/benzophenone, sodium, or calcium hydride as appropriate. All standards and test samples were handled under an inert atmosphere (N<sub>2</sub>) in a drybox, with the exception of CuO, which was handled in air. Solution <sup>1</sup>H NMR spectra were recorded at ambient temperature on a Bruker AMX300 spectrometer at 300 MHz or on a Bruker AMX400 spectrometer at 400 MHz. Benzene-*d*<sub>6</sub>, vacuum transferred from a Na/K alloy, was used as the solvent for all NMR studies. Infrared spectra were recorded using a Mattson Infinity Series FTIR spectrometer with all samples pressed into KBr disks under inert atmosphere in a drybox. Thermogravimetric analysis (TGA) measurements were performed using a TA Instruments SDT 2960 integrated thermogravimetric/differential scanning calorimetric analyzer (TGA/DSC). A Quantachrome Autosorb-One was used for N<sub>2</sub> porosimetry measurements. The Brunauer–Emmet–Teller (BET) method<sup>19</sup> was used to determine the surface area, and the Barrett–Joyner–Halenda (BJH) method<sup>20</sup> was used to obtain the pore-size distribution. Powder X-ray diffraction (PXRD) data were collected using a Siemens D5000 diffractometer with Cu K $\alpha$  radiation. The Cu and Cl contents (where appropriate) of the materials studied were measured by Galbraith Laboratories, Knoxville, TN, using ionization coupled plasma methods.  $[\text{CuO}^t\text{Bu}]_4$ <sup>17</sup> and  $[\text{CuOSi}(\text{O}^t\text{Bu})_3]_4$ <sup>16</sup> were synthesized by literature methods, and Si(OEt)<sub>4</sub>, Cu<sub>2</sub>O, CuO, and CuCl were purchased from Aldrich and used as received. The mesoporous silica support, SBA-15, was prepared according to literature procedures<sup>16</sup> and characterized by PXRD and N<sub>2</sub> porosimetry (area, 894 m<sup>2</sup> g<sup>-1</sup>; pore volume, 1.13 cm<sup>3</sup> g<sup>-1</sup>; average pore diameter, 77 Å). The hydroxyl group concentration of the SBA-15 was determined to be 1.3(1) OH nm<sup>-2</sup>, via reaction of the SBA-15 material with Mg(C<sub>6</sub>H<sub>5</sub>CH<sub>2</sub>)<sub>2</sub>·2THF and quantification of the toluene evolved by <sup>1</sup>H NMR spectroscopy.<sup>21</sup>

**Preparation of SBA-15-Supported Cu.** The materials prepared via grafting using molecular precursors ( $[\text{CuOSi}(\text{O}^t\text{Bu})_3]_4$  and  $[\text{CuO}^t\text{Bu}]_4$ ) are identified in the following manner. Materials prepared using  $[\text{CuOSi}(\text{O}^t\text{Bu})_3]_4$  and  $[\text{CuO}^t\text{Bu}]_4$  are designated as CuOSi/SBA (*x.x*) and CuO<sup>t</sup>Bu/SBA (*x.x*), respectively. In each case, (*x.x*) indicates the weight loading (%) of Cu after removal of the organic components of the ligands (i.e., after loss of *n*CH<sub>2</sub>C(CH<sub>3</sub>)<sub>2</sub> and <sup>*n*</sup>/2H<sub>2</sub>O upon heating to ca. 473 K). Grafting of the molecular precursors was carried out according to the following representative example. Dry SBA-15 (1.000 g, 1.93 mmol of OH) was suspended in C<sub>6</sub>H<sub>6</sub> (15 mL) in a Schlenk tube under an inert atmosphere (N<sub>2</sub>). While the SBA-15 suspension was being stirred rapidly, a clear yellow solution of  $[\text{CuOSi}(\text{O}^t\text{Bu})_3]_4$  (0.206 g, 0.158 mmol) in C<sub>6</sub>H<sub>6</sub> (15 mL) was added via cannula transfer at 298 K. The solid

SBA-15 turned to a pale yellow color immediately. The yellow suspension was stirred at 298 K for 1 h under flowing N<sub>2</sub> and allowed to settle. The clear and colorless C<sub>6</sub>H<sub>6</sub> was transferred, via cannula filtration, to another Schlenk tube under N<sub>2</sub> (set aside for later use). The light yellow residue was thoroughly washed (with stirring) using three 10 mL portions of dry C<sub>6</sub>H<sub>6</sub>, with each wash leading to a clear and colorless filtrate (combined with the previous filtrate sample). A light yellow gelatinous material remained after the final filtration step (still slightly wet). The final material was dried under reduced pressure at 298 K for 30 min, 323 K for 30 min, and 333 K for 2.5 h. The light yellow dry material (CuOSi/SBA (3.5)) was brought into an inert-atmosphere drybox (N<sub>2</sub>), isolated (1.086 g), and stored under N<sub>2</sub> for future use.

The clear and colorless solvent from the filtrate fractions (still under N<sub>2</sub>) was removed under reduced pressure at 298 K. The colorless solid residue that remained was taken up in C<sub>6</sub>D<sub>6</sub> and analyzed by <sup>1</sup>H NMR spectroscopy using Cp<sub>2</sub>Fe as a standard. The only reaction product detected was HOSi(O<sup>t</sup>Bu)<sub>3</sub> (0.159 mmol; 1 molecule per molecule of  $[\text{CuOSi}(\text{O}^t\text{Bu})_3]_4$ ). Neither  $[\text{CuOSi}(\text{O}^t\text{Bu})_3]_4$  nor <sup>t</sup>BuOH was detected. Monitoring the progress of similar grafting reactions in situ by <sup>1</sup>H NMR spectroscopy (C<sub>6</sub>D<sub>6</sub>) also revealed that HOSi(O<sup>t</sup>Bu)<sub>3</sub> was the only organic reaction product given off, with no unreacted  $[\text{CuOSi}(\text{O}^t\text{Bu})_3]_4$  or <sup>t</sup>BuOH detected.

Similar procedures to those described above for the generation of CuOSi/SBA (3.5) were used to form CuOSi/SBA (5.0), CuO<sup>t</sup>Bu/SBA (3.5), and CuO<sup>t</sup>Bu/SBA (5.0). For the  $[\text{CuO}^t\text{Bu}]_4$  materials, 1 equiv of <sup>t</sup>BuOH was evolved per molecule of  $[\text{CuO}^t\text{Bu}]_4$  reacted with the SBA-15, as expected.

A sample of 3 wt % Cu on SBA-15 was also prepared by the high-temperature reaction of dry SBA-15 with CuCl. This sample is designated as CuCl/SBA (3.0). In a drybox (N<sub>2</sub>), 0.500 g (0.965 mmol “OH”) of SBA-15 was transferred to a quartz tube (2.5 cm i.d.) fitted with a frit and gastight poly(tetrafluoroethylene) (PTFE) valves. A concentric quartz tube (1.9 cm i.d.) containing 0.058 g (0.59 mmol) of CuCl on a quartz frit was positioned above the bed of SBA-15. The system was then sealed under N<sub>2</sub>, brought to a furnace, heated under flowing N<sub>2</sub> (50 cm<sup>3</sup> min<sup>-1</sup>) at a rate of 5 K min<sup>-1</sup> to 893 K, and subsequently held isothermal for 50 h. The final light yellow material (CuCl/SBA (3.0)) was isolated in a drybox and stored for future use. The CuCl amount required to obtain a weight loading of ca. 3% was determined empirically. It was found that not all of the Cu from the CuCl was incorporated because of condensation of CuCl below the SBA-15 bed and outside the heated region of the furnace.

**X-ray Absorption Spectroscopy (XAS).** EXAFS and XANES measurements were performed at the Stanford Synchrotron Radiation Laboratory (SSRL) and the National Synchrotron Light Source (NSLS). Cu K edge absorption measurements were performed on beamline 6-2 at SSRL and on beamline X11A at NSLS. Both beamlines were equipped with a Si(111) double crystal monochromator; no additional optics were used. The premonochromator vertical aperture of the beams was set to 0.5 mm for improved resolution,<sup>22</sup> defining an energy resolution of 1.8 eV. The monochromator was detuned 20–30% at 400 eV above the Cu K edge to attenuate the flux from higher-order Bragg diffractions. Cu metal foil (7 μm) was used for energy calibration and changes in beam alignment.

In addition to the Cu-containing SBA-15 supported materials, XANES and EXAFS data were collected for five standards (CuCl, Cu<sub>2</sub>O, CuO,  $[\text{CuO}^t\text{Bu}]_4$ , and  $[\text{CuOSi}(\text{O}^t\text{Bu})_3]_4$ ). Each sample was pressed into a rectangular pellet (0.43 cm × 1.86

cm, with the thickness dependent upon the amount of sample used) and loaded into an in situ cell for transmission experiments.<sup>23</sup> Sufficient quantity of each sample was used (typically 5–10 mg for standards and 50–80 mg for samples) to give a calculated optical density ( $\mu_{\text{m}}\rho x$ ) of 2.<sup>24</sup> The cell was evacuated to  $10^{-6}$  Torr, and the sample holder was cooled by liquid nitrogen during the experiment. Intensities of the beam were measured over a 900 eV range using a sampling step of 5 eV in the preedge and 0.3 eV in the XANES region (−30 to 30 eV relative to  $E_0$ ) with a 1 s hold at each step. The EXAFS region was taken from 30 eV to 12 k in 0.05 k steps and from 12 to 16 k in 0.07 k steps holding for 2 and 3 s, respectively. The frequency of data points in the EXAFS region was chosen to satisfy the Nyquist theorem.<sup>24a</sup> Ionization chambers ( $\text{N}_2$  filled) were used to measure the incident and sample transmitted fluxes. A third detector was used to measure the flux through a (7  $\mu\text{m}$  thick) Cu foil internal standard. Three to five scans were taken per sample to improve the signal-to-noise ratio.

A portable flow manifold was used to treat each material on site. Each sample was first treated in He (99.999%) at a flow rate of  $60\text{ cm}^3\text{ min}^{-1}$ . An Omega CN2250 temperature controller was used to ramp the temperature at  $10\text{ K min}^{-1}$  to 573 K and maintain it at this temperature for 2 h in order to facilitate removal of residual organic species from the CuO/Bu/SBA (x.x) and CuOSi/SBA (x.x) materials. For consistency, CuCl/SBA (3.0) was treated in the same manner. After characterization by XAS, each He treated sample was heated in flowing  $\text{O}_2$  (10%, balance He,  $60\text{ cm}^3\text{ min}^{-1}$ ). The temperature was ramped at  $10\text{ K min}^{-1}$  to 773 K and held at this temperature for 1 h. The sample cell was then cooled for 20–30 min to 293 K and evacuated to ca.  $10^{-6}$  Torr.

**X-ray Absorption Near-Edge Structure (XANES) Analyses.** XANES analyses were carried out using the WinXAS (version 2.3) software.<sup>25</sup> The energy was calibrated using the Cu K edge of the Cu foil, which was taken as 8980 eV. Preedge absorptions due to the background and detector were subtracted using a linear fit to the data in the range of −200 to −50 eV relative to the sample edge energy ( $E_0$ ). Each spectrum was then normalized by a constant determined by the average absorption in the range of 100–300 eV relative to  $E_0$ . The edge energy of each sample and reference was taken at the first inflection point beyond any preedge peaks. Because of a larger than optimal premonochromator slit height, the energy resolution for CuOSi/SBA (5.0) and CuO/Bu/SBA (3.5) is greater than 2 eV. Hence, subtle electronic transitions in the edge region could not be resolved from the main edge feature. Low resolution in the XANES region does not adversely affect the quality of EXAFS data, as it is known that EXAFS features oscillate much more slowly than the energy width.<sup>24</sup> Because of the limited availability of synchrotron beamtime, well-resolved XANES data were collected only for CuOSi/SBA (3.5), CuO/Bu/SBA (5.0), CuCl/SBA (3.0), and all standards.

**EXAFS Analyses.** Extraction and fitting of the EXAFS function,  $\chi(k)$ , was done with the aid of the UWXAFS<sup>26</sup> suite of software programs and its GUI-based equivalent, IFEFFIT.<sup>27</sup> An identical approach was taken in the workup of the raw absorption data. The preedge absorptions were subtracted using a linear fit to the data in the range of −200 to −50 eV relative to  $E_0$ .  $E_0$  was defined as the first inflection point on the rising absorption edge. For all of the Cu-containing samples studied, this inflection point was on the lower third of the absorption step. Each spectrum was normalized as described above.

Special attention was given to modeling the atomic absorption background. The AUTOBK<sup>28</sup> algorithm was used to select spline

points between a  $k$  of 1.5 and  $15\text{ \AA}^{-1}$ , where  $k$  is the wave vector.<sup>24</sup> As defined by AUTOBK, an  $R_{\text{bkg}}$  value of 1.0 was chosen. These parameters minimized the magnitude of unphysical Fourier peaks below  $1\text{ \AA}$  present in the Fourier transform of the  $k^3$ -weighted scattering function,  $\chi(k)$  (FT  $k^3\chi(k)$ ) (uncorrected for total phase shift).

Fourier transforms (FT) were performed on the  $k^3$ -weighted  $\chi(k)$  functions. All figures showing FT  $k^3\chi(k)$  data are plotted without phase correction. The  $k$  range of the transform varied between a  $k_{\text{min}}$  of 2.0–3.0  $\text{\AA}^{-1}$  and a  $k_{\text{max}}$  of 11.5–14.0  $\text{\AA}^{-1}$  for all spectra. The  $k_{\text{min}}$  and  $k_{\text{max}}$  values were chosen at node points to help minimize spectral broadening. Values of  $k_{\text{min}}$  below 2.0 were avoided because multiple scattering often becomes more important in this energy region.<sup>24b,c</sup> All spectra were transformed with a Hanning window function using a windowsill ( $dk$ ) of  $1\text{ \AA}^{-1}$  centered on the chosen nodal position. Side lobes or feet associated with the first Fourier peak often occurred despite the use of the Hanning apodization function used in the numerical transform. A sine function was used to achieve more severe apodization so as to confirm that side peaks were artifacts rather than real Fourier components.<sup>29</sup> However, the sine windowing function was not used in the presentation or fitting of the data because it minimized side lobes at the expense of broadening real spectral components.

The EXAFS scattering function,  $\chi(k)$ , is given by eq 1.<sup>24b,c</sup> In the equation,  $N_j$  is the number of atoms in shell  $j$  at a particular distance  $R_j$ . The argument inside the sine function contains the phase shifts ( $\phi_j(k)$ ) for the absorber and backscatterer.  $F_j(k)$  is the effective backscattering amplitude function for atoms in the  $j^{\text{th}}$  shell.  $S_0^2$  is the many-body amplitude reduction factor,  $\sigma^2$  is the harmonic Debye–Waller factor, and  $\lambda$  is the mean-free path of the electron, which is often incorporated into  $S_0^2$  for the sake of modeling.

$$\chi(k) = \sum_{j=1}^{\text{Shells}} \frac{N_j}{k R_j^2} S_0^2 F_j(k) e^{-2k^2\sigma_j^2} e^{-2R_j/\lambda(k)} \sin[2kR_j - \phi_j(k)] \quad (1)$$

$S_0^2$  was extracted by fitting the first peak in FT  $k^3\chi(k)$  for Cu foil, using the theoretical values of  $F_j(k)$  and  $\phi_j(k)$  determined by the FEFF 8.2 code.<sup>30</sup> The fit was done in back FT  $k$  space and in  $R$  space. A value of  $S_0^2 = 0.865$  was obtained in both refinements, and this value was used in all subsequent analyses.

For the sample fittings, theoretical amplitude and phase functions were calculated for all Cu–O, Cu–Cu, and Cu–Si coordination environments using scattering paths obtained from atomic coordinates of the standards reported. Atomic coordinates for Cu metal, CuO,  $\text{Cu}_2\text{O}$ , and CuCl are known,<sup>31</sup> as are the crystallographic coordinates for  $[\text{CuO/Bu}]_4$ .<sup>32</sup> The atomic coordinates for  $[\text{CuOSi(O'Bu)}_3]_4$  are not known; however, those for  $[\text{CuOSi(O'Bu)}_2\text{C}_6\text{H}_5]_4$ , a close structural relative,<sup>17</sup> are available and were used. Relevant scattering contributions for all standards were considered initially, but final fits were determined using Cu foil for Cu–Cu interactions, CuO for Cu–O and Cu–Cu interactions, and  $[\text{CuOSi(O'Bu)}_3]_4$  for Cu–Si interactions, unless otherwise stated. All FEFF paths were calculated considering self-consistent potentials (Hedin–Lundqvist),  $\sigma^2 = 0$ , and  $S_0^2 = 1$ . The generated spectra were referenced to the threshold Fermi level with a reported error of ca. 1 eV using self-consistent calculations.<sup>33</sup>

All fits of the samples and standards were performed on the real and imaginary parts of the FT  $k^3\chi(k)$  data. The  $k$  and  $R$  ranges of all the sample fits and the number of independent points available for least-squares optimization are listed in Table 1. Two to three shells were fit simultaneously allowing  $\sigma$ ,  $R_j$ ,



TABLE 1:  $k$  Space and  $R$  Space Range for Fitting

material	treatment	$k_{\min}$ ( $\text{\AA}^{-1}$ )	$k_{\max}$ ( $\text{\AA}^{-1}$ )	$\Delta k$	$R_{\min}$ ( $\text{\AA}$ )	$R_{\max}$ ( $\text{\AA}$ )	$\Delta R$	$N_{\text{ind}}^a$
CuCl/SBA (3.0)	fresh	2.0	12.5	10.5	1.2	1.9	0.7	6.7
		2.0	12.5	10.5	1.9	2.9	1.0	8.7
	helium	3.0	12.8	9.8	1.1	2.4	1.3	10.1
	oxygen	3.0	13.5	10.5	1.3	3.3	2.0	15.4
CuOSi/SBA (3.5)	fresh	2.0	12.6	10.6	1.2	3.0	1.8	14.1
	helium	3.0	14.0	11.0	1.2	2.5	1.3	11.1
CuOSi/SBA (5.0)	fresh	2.0	12.5	10.5	1.2	2.9	1.7	13.4
	helium	2.8	14.2	11.4	1.2	3.5	2.3	18.7
	oxygen	2.8	13.3	10.5	1.2	2.9	1.7	13.4
CuOtBu/SBA (3.5)	fresh	2.8	12.1	9.3	1.2	2.9	1.7	12.1
	helium	2.7	14.2	11.5	1.8	3.6	1.8	15.2
CuOtBu/SBA (5.0)	fresh	2.8	12.3	9.5	1.2	2.8	1.6	11.7
	helium	2.6	13.0	10.4	1.8	3.5	1.7	13.3
	oxygen	2.9	13.4	10.5	1.2	3.3	2.1	16.0

<sup>a</sup> Number of independent data points ( $N_{\text{ind}}$ ) in fit calculated by  $N_{\text{ind}} = (2\Delta k\Delta R/\pi) + 2$ ,

and  $N_j$  to be adjusted for each Fourier component. A single edge shift correction ( $\Delta E_0$ ) was refined for each fit, unless reported otherwise. Multiscattering contributions were attempted only for the spectra of the He treated samples.

The quality of a particular fit was evaluated by use of the reduced chi-square method ( $\chi^2_r$ ).<sup>34</sup> Once a best fit was found, the  $\mathcal{R}$ -factor was recorded for presentation of the fits. Because the fits were done in FT  $R$  space, the  $\mathcal{R}$ -factor is defined as shown in eq 2, where  $f_i = \tilde{\chi}_{\text{data}}(R_i) - \tilde{\chi}_{\text{model}}(R_i)$  and  $N = 2(R_{\text{max}} - R_{\text{min}})/\Delta R$  is the total number of evaluations with one real and one imaginary evaluation at each point. This factor gives a sum-of-square measure of the fractional misfit.<sup>34</sup> The numbers reported for all uncertainties in the fit variables have been estimated using a standard technique of error analysis such as the Levenberg–Marquardt algorithm. More details are available in ref 34. The significant digit of the uncertainty is shown adjacent to the fitted value.

$$\mathcal{R} = \frac{\sum_{i=1}^N \{[\text{Re}(f_i)]^2 + [\text{Im}(f_i)]^2\}}{\sum_{i=1}^N \{[\text{Re}(\tilde{\chi}_{\text{data}}(R_i))]^2 + [\text{Im}(\tilde{\chi}_{\text{data}}(R_i))]^2\}} \quad (2)$$

## Results and Discussion

Both the surface area and the pore volume of freshly prepared CuOSi/SBA (3.5) ( $678 \text{ m}^2 \text{ g}^{-1}$  and  $0.88 \text{ cm}^3 \text{ g}^{-1}$ ) were reduced when compared to the values for the SBA-15 support ( $894 \text{ m}^2 \text{ g}^{-1}$  and  $1.13 \text{ cm}^3 \text{ g}^{-1}$ ), although the mesostructured nature of the material was maintained. Interestingly, after thermolysis at 673 K under flowing  $\text{N}_2$ , both the surface area and the pore volume of CuOSi/SBA (3.5) increased ( $800 \text{ m}^2 \text{ g}^{-1}$  and  $1.01 \text{ cm}^3 \text{ g}^{-1}$ ). Thus, the porosimetry data suggest that detection of the pore filling by the bulky molecular precursor is possible and that thermolysis reduces the space occupied by the grafted species upon evolution of the organic groups. The Cu content measured after loss of all organics species is presented in Table 2.

Reaction of SBA-15 with excess CuCl at 873 K afforded CuCl/SBA (3.0) as a light yellow powder. Attempts to obtain higher loadings of Cu were met with limited success, with increasingly large amounts of excess CuCl being required for minimal gains in Cu loading. The Cu and Cl content of CuCl/SBA (3.0) after treatment under He at 573 K are presented in

TABLE 2: Materials Analysis

materials <sup>a</sup>	Cu (wt %)	Cl (wt %)	Cu/Cl (atom)
CuCl/SBA (3.0)	2.92	0.35	4.6
CuSiO/SBA (5.0)	5.21		
CuSiO/SBA (3.5)	3.61		
CuO'Bu/SBA (5.0)	4.31		
CuO'Bu/SBA (3.5)	3.35		

<sup>a</sup> Values are for He treated samples at 573 K. The error is approximately  $\pm 10\%$ .

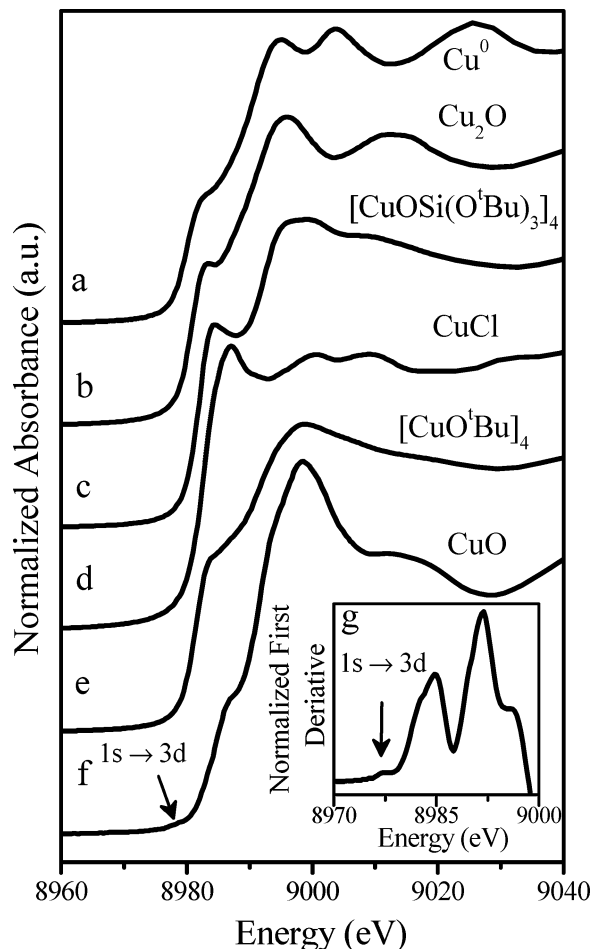


**Figure 1.** Cu K edge XANES spectra of Cu reference materials: (a) Cu foil, (b)  $\text{Cu}_2\text{O}$ , (c)  $[\text{CuOSi}(\text{O}^t\text{Bu})_3]_4$ , (d) CuCl, (e)  $[\text{CuO}^t\text{Bu}]_4$ , (f) CuO, and (g) first derivative absorbance of CuO.

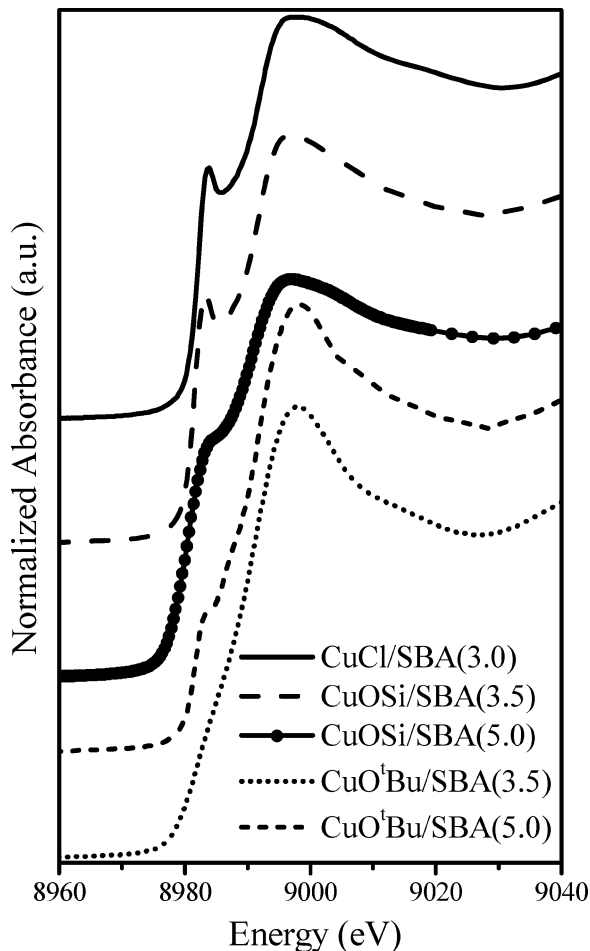
Table 2. Both the surface area and pore volume of freshly prepared CuCl/SBA (3.0) ( $600 \text{ m}^2 \text{ g}^{-1}$  and  $0.8 \text{ cm}^3 \text{ g}^{-1}$ ) were lower than the values obtained for SBA-15; however, the 100, 110, and 200 diffraction planes were of similar intensity, indicating maintenance of the mesoporous structure after the high-temperature treatment with excess CuCl at 873 K. Elemental analysis of CuCl/SBA (3.0) shows that it contains residual Cl (Cl/Cu = 1:4.6).

**XANES: Standards and Samples.** The XANES spectrum of each standard is shown in Figure 1. Edge energies and energies for specific electronic transitions are listed in Table 3. For Cu metal ( $3d^{10}4s$ ), the first peak on the rising edge at 8982.4 eV is assigned to the  $1s \rightarrow 4p$  transition. The  $4p$  states of pure Cu metal are more diffuse because of hybridization with  $4s$  and  $3d$  states.<sup>35</sup> A single absorption peak in the range 8983–8985 eV for  $\text{Cu}_2\text{O}$ , CuCl, and  $[\text{CuOSi}(\text{O}^t\text{Bu})_3]_4$  is assigned to the electric dipole-allowed transition characteristic of  $\text{Cu}^{\text{I}}$  ( $3d^{10}$ ) samples. This absorption feature is not clearly present in the

**TABLE 3: Edge Energy and Relevant Electronic Transitions Energies for Standards**

standard	formal valency	$E_0^a$ (eV)	$1s \rightarrow 4p^b$ (eV)	$1s \rightarrow 4p_{xy}^c$ (eV)	$1s \rightarrow 3d^d$ (eV)
Cu foil	0	8980.0	8995.1		
[CuOSi(O'Bu) <sub>3</sub> ] <sub>4</sub>	1	8982.1	8999.0	8984.7	
[CuO'Bu] <sub>4</sub>	1	8981.5	8998.9	8984.0 <sub>e</sub>	
CuCl	1	8982.8	9000.7	8987.2	
Cu <sub>2</sub> O	1	8980.8	8996.0	8983.5	
CuO	2	8984.5	8998.7		8977.8

<sup>a</sup> Edge energy defined as the first inflection point on the rising absorption edge. <sup>b</sup> Energy position at maximum absorption. <sup>c</sup> Energy at edge peak associated with Cu<sup>I</sup>. <sup>d</sup> Weak preedge peak associated with Cu<sup>II</sup> defined at inflection point of peak. <sup>e</sup> Energy at shoulder; energy taken at second inflection point on rising absorption edge.

**Figure 2.** XANES spectra of freshly prepared materials.

XANES spectrum of [CuO'Bu]<sub>4</sub>, but the edge energy indicates that Cu is present as Cu<sup>I</sup>. CuO has two distinguishable features characteristic of Cu<sup>II</sup> (3d<sup>9</sup>) compounds. There is a subtle preedge absorption at 8978 eV corresponding to the  $1s \rightarrow 3d$  dipole-forbidden transition, and there is a shoulder at 8986 eV attributed to the  $1s \rightarrow 4p$  “shake down” transition.<sup>35,36</sup> The absorption at 8978 eV is easier to resolve in the first-derivative absorption spectrum (Figure 1f). Because of covalent bonding and hybridization of the p and d orbitals, this absorption is often correlated to the symmetry of the site.<sup>35,36</sup>

Normalized XANES spectra of freshly prepared CuO'Bu/SBA (3.5), CuO'Bu/SBA (5.0), CuOSi/SBA (3.5), CuOSi/SBA (5.0), and CuCl/SBA (3.0) are shown in Figure 2. Edge energies and energies for specific electronic transitions for freshly prepared and He and O<sub>2</sub> treated samples are listed in Table 4. The edge energies observed for all freshly prepared samples lie in the

**TABLE 4: Edge Energy and Relevant Electronic Transitions Energies for Fresh and Pretreated Samples**

material	treatment conditions	$E_0^a$ (eV)	$1s \rightarrow 4p^b$ (eV)	$1s \rightarrow 4p_{xy}^c$ (eV)	$1s \rightarrow 3d^d$ (eV)
CuCl/SBA (3.0)	fresh	8981.9	8996.7	8983.6	
CuSiO/SBA (3.5)		8982.1	8998.5	8984.5	
CuSiO/SBA (5.0) <sup>e</sup>		8980.7	8998.4	<i>e</i>	
CuOtBu/SBA (3.5) <sup>e</sup>		8982.3	8997.8	<i>f</i>	
CuOtBu/SBA (5.0)		8981.7	8998.2	8983.7	
CuCl/SBA (3.0)	He 573 K (1 h)	8982.5	8995.9	8984.1	
CuSiO/SBA (3.5)		8981.7	8996.2	8983.5	
CuSiO/SBA (5.0) <sup>e</sup>		8980.7	8996.9	<i>e</i>	
CuOtBu/SBA (3.5) <sup>e</sup>		8979.4	8995.9		
CuOtBu/SBA (5.0)		8979.5	8995.5		
CuCl/SBA (3.0)	O <sub>2</sub> 773 K (1 h)	8984.6	8998.3		8977.0
CuSiO/SBA (5.0)		8985.7	8998.5		8976.7
CuOtBu/SBA (5.0)		8985.6	8998.2		8977.0

<sup>a</sup> Edge energy defined as the first inflection point on the rising absorption edge. <sup>b</sup> Energy position at maximum absorption. <sup>c</sup> Energy at edge peak associated with Cu<sup>I</sup>. <sup>d</sup> Weak preedge peak associated with Cu<sup>II</sup> defined at inflection point of peak. <sup>e</sup> Energy resolution estimated to be greater than 2 eV.

range characteristic for Cu<sup>I</sup> species (8980.5–8982.5).<sup>35,36c</sup> Also, the XANES spectra of CuO'Bu/SBA (5.0), CuOSi/SBA (3.5), and CuCl/SBA (3.0) exhibit a peak for the  $1s \rightarrow 4p_{xy}$  transition between 8983 and 8984 eV, which is characteristic of Cu<sup>I</sup>.<sup>35,36f</sup> CuO'Bu/SBA (3.5) and CuOSi/SBA (5.0) do not have noticeable edge peaks between 8983 and 8984 eV because of the low resolution with which these particular spectra were collected.<sup>22</sup>

The XANES spectra of CuOSi/SBA (3.5), CuOSi/SBA (5.0), CuO'Bu/SBA (3.5), CuO'Bu/SBA (5.0), and CuCl/SBA (3.0) after He treatment at 573 K for 1 h are shown in Figure 3. The edge energies for CuOSi/SBA (3.5), CuOSi/SBA (5.0), and CuCl/SBA (3.0) lie within the range expected for Cu<sup>I</sup> species,<sup>35,36c</sup> whereas those for CuO'Bu/SBA (3.5) and CuO'Bu/SBA (5.0) lie in the range characteristic of Cu<sup>0</sup> (Table 4). Evidence for metallic Cu is also suggested by the presence of a broad peak above 9020 eV in the spectra of these latter samples.<sup>7c</sup> The spectra of CuOSi/SBA (3.5) and CuCl/SBA (3.0) exhibit well-resolved edge features at 8983.5 and 8984.1 eV, respectively, typical of the  $1s \rightarrow 4p_{xy}$  transition for Cu<sup>I</sup>. A similar feature is observed in the spectrum of CuSiO/SBA (5.0) but is not as well resolved as in the spectrum of CuOSi/SBA (3.5).<sup>22</sup>

The XANES spectra of CuOSi/SBA (5.0), CuO'Bu/SBA (5.0), and CuCl/SBA (3.0) after O<sub>2</sub> treatment at 773 K are shown in Figure 4. Each of these spectra exhibits an edge energy at ca. 8985 eV and  $1s \rightarrow 3d$  transition energies that are representative of fully oxidized Cu<sup>II</sup> species (Table 4).

**EXAFS: Standards.** Normalized, atomic background-subtracted  $k^3$ -weighted scattering functions ( $k^3\chi(k)$ ) for all standards are shown in Figure 5a, and the corresponding FTs are shown in Figure 5b. The signal-to-noise ratios and overall quality of the spectra are good, as is expected for well-ordered materials at cryogenic temperatures. Of particular interest are the previously unknown EXAFS data for [CuO'Bu]<sub>4</sub> and [CuOSi(O'Bu)<sub>3</sub>]<sub>4</sub>. The central [Cu–O]<sub>4</sub> ring of both complexes is essentially identical. Differences in the nature of the ligands bound to Cu (i.e., –OSi(O'Bu)<sub>3</sub> versus –O'Bu) are the primary reasons for the shoulders and splitting observed at ca. 5.0, 9.2, and 12.0 Å<sup>–1</sup> in the EXAFS spectrum of [CuOSi(O'Bu)<sub>3</sub>]<sub>4</sub> as compared to that of [CuO'Bu]<sub>4</sub>. The –OSi(O'Bu)<sub>3</sub> ligand highlights an important difference between the precursors and provides realistic Cu–Si scattering paths that can be used to interpret EXAFS data in the Cu-containing materials discussed here.

The forward FT  $k^3\chi(k)$  for [CuOSi(O'Bu)<sub>3</sub>]<sub>4</sub> shows remarkable agreement with the FEFF generated FT  $k^3\chi(k)$  simulation of

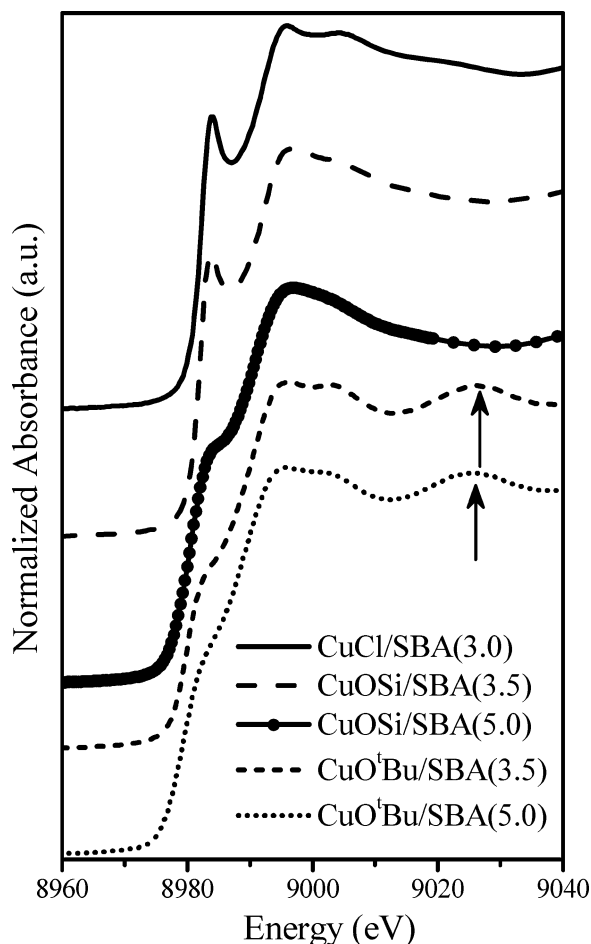


**Figure 3.** XANES spectra of materials after treatment at 573 K in He for 1 h.

[CuOSi(O<sup>t</sup>Bu)<sub>3</sub>]<sub>4</sub> (Figure 6a). As noted earlier, the atomic coordinates of Cu, O, and Si necessary for the simulation of [CuOSi(O<sup>t</sup>Bu)<sub>3</sub>]<sub>4</sub> were taken from X-ray crystal data of the related complex [CuOSi(O<sup>t</sup>Bu)<sub>2</sub>C<sub>6</sub>H<sub>5</sub>]<sub>4</sub>.<sup>17</sup> The differences in the simulation between [CuOSi(O<sup>t</sup>Bu)<sub>3</sub>]<sub>4</sub> and [CuOSi(O<sup>t</sup>Bu)<sub>2</sub>C<sub>6</sub>H<sub>5</sub>]<sub>4</sub> are expected to be negligible because of the weak backscattering amplitude of carbon in the two complexes.<sup>24d</sup> The FT of the FEFF simulation was done using transform parameters identical to those used for the experimental data. All scattering paths less than 4.5 Å in length were included in the FEFF simulation. On the basis of a path-by-path analysis, the peaks (nonphase corrected) appearing at 1.45, 2.3, and 3.65 Å in Figure 6a can be assigned to Cu–O, Cu–Cu (adjacent), and Cu–Cu (across) backscattering, respectively. The shoulder at 2.8 Å is attributed to Cu–Si backscattering, whereas the peak at 3.2 Å is associated with small-amplitude Cu–C, Cu–O, and multiple scattering contributions. Because the theoretical phase and amplitude functions were calculated using ideal parameters of  $\sigma^2 = 0$  Å<sup>2</sup> and  $S_0^2 = 1$ , a more physically meaningful model was constructed by trial and error to achieve good agreement between experiment and theory at 2.3 Å. The resulting model is shown in Figure 6a for a  $\sigma^2 = 0.0035$  Å<sup>2</sup> and  $S_0^2 = 0.864$  (as determined by fit to Cu foil).

Further confirmation of the selection of appropriate scattering paths can be obtained from an examination of the imaginary part of FT  $k^3\chi(k)$ , which carries element-specific phase shift variations.<sup>37</sup> To obtain this information, a peak or combination of peaks must be well isolated. For [CuOSi(O<sup>t</sup>Bu)<sub>3</sub>]<sub>4</sub>, the peaks due to Cu–Cu and Cu–Si scattering paths are separable (Figure 6b). Therefore, these paths were simulated, and their contribution

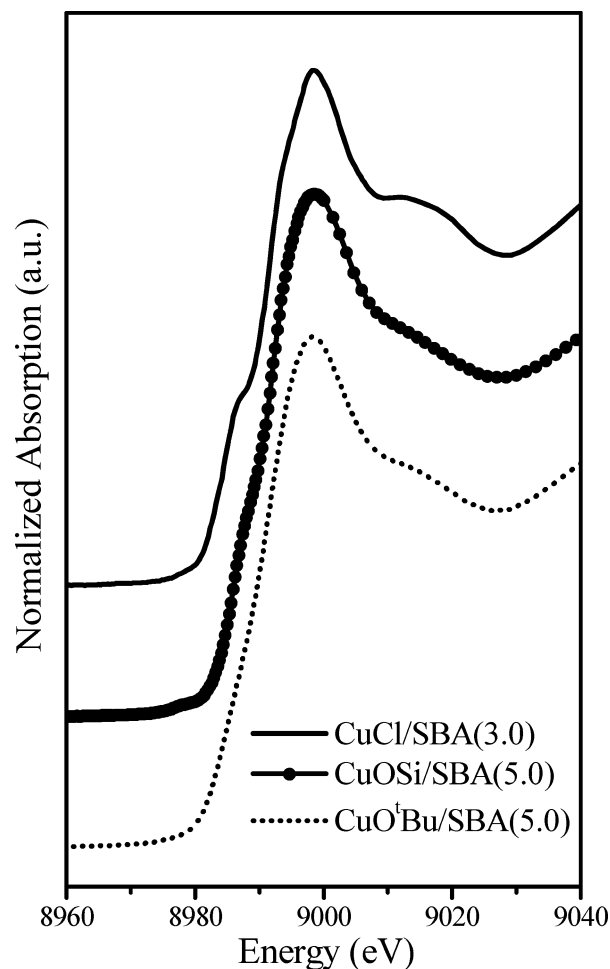


**Figure 4.** XANES spectra of materials after treatment at 773 K in O<sub>2</sub> for 1 h.

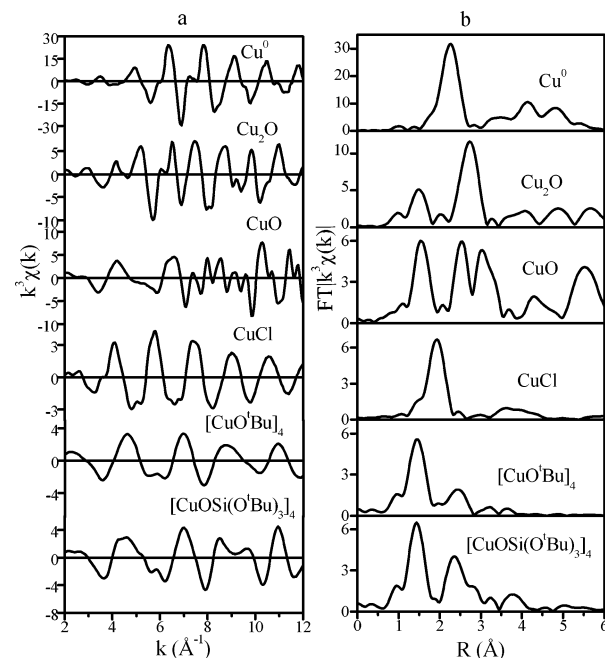


**Figure 5.** (a) Normalized and background subtracted  $k^3\chi(k)$  spectra of standards. (b) Forward Fourier transforms of the spectra are nonphase corrected.

to  $\chi(k)$  were added before taking the forward FT of  $k^3\chi(k)$  (Figure 6b, inset). As observed in Figure 6c, there is remarkable agreement in the shape, number of peaks, and the phase of the

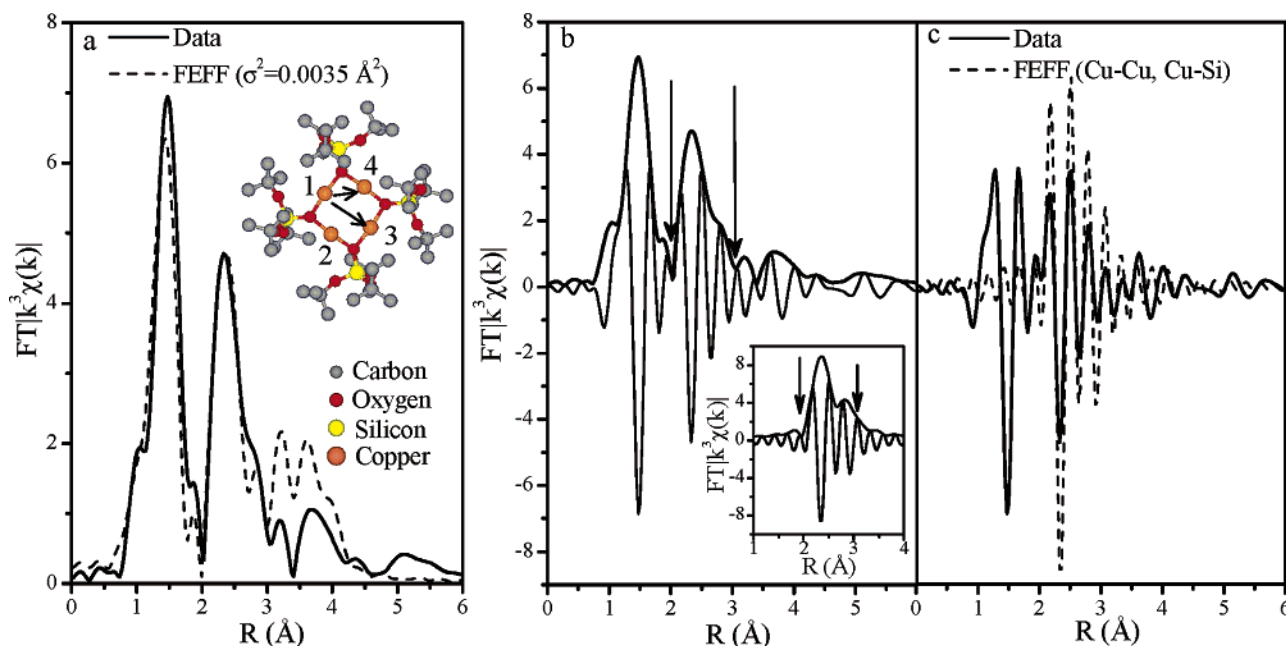


**Figure 6.** (a) Comparison of FEFF 8.2 simulation of  $[\text{CuOSi}(\text{O}^+\text{Bu})_3]_4$  with experimental data assuming  $\sigma^2 = 0.0035 \text{ \AA}^2$ . Inset shows structure of  $[\text{CuOSi}(\text{O}^+\text{Bu})_3]_4$ . Copper atoms are labeled 1–4. Cu1–Cu2 (Cu1–Cu4) are “adjacent” copper scatterers, whereas Cu1–Cu3 are “across” copper scatterers. (b) Magnitude and imaginary part of the Fourier transformed  $k^3\chi(k)$  of  $[\text{CuOSi}(\text{O}^+\text{Bu})_3]_4$ . The inset shows FEFF simulation of combined Cu–Cu and Cu–Si nearest-neighbor scattering of  $[\text{CuOSi}(\text{O}^+\text{Bu})_3]_4$ . Arrows bracket Fourier components of Cu–Cu and Cu–Si scattering in both the data and the simulation. (c) Overlay of the data and FEFF simulation ( $\sigma^2 = 0.0 \text{ \AA}^2$ ) of the imaginary part for Cu–Cu and Cu–Si scattering contributions.

**TABLE 5: Fitting Results for  $[\text{CuOSi}(\text{O}^+\text{Bu})_3]_4$  and  $[\text{CuO}^+\text{Bu}]_4$**

precursor	shell	CN <sup>c</sup>	$R \text{ (\AA)}^d$	$\sigma^2 \text{ (\AA}^2)^e$	$E_0 \text{ (eV)}^f$	$R\text{-factor}^g$	XRD <sup>h,g</sup>	
							CN	$R \text{ (\AA)}$
$[\text{CuOSi}(\text{O}^+\text{Bu})_3]_4^a$	Cu–O	2	1.838(4)	0.0021(3)			2	1.842(4), 1.828(5)
	Cu–Cu	2	2.716(5)	0.0062(3)	0.9(1.0)	0.0098	2	2.675(1), 2.764(1)
	Cu–Si	2	3.138(1)	0.0054(1)			2	3.132, 3.139
	Cu–Cu	1	3.92(3)	0.0065(8)	12.9(5.1)	0.0376	1	3.861
$[\text{CuO}^+\text{Bu}]_4^b$	Cu–O	2	1.853(2)	0.0024(1)	0.7(6)	0.0031	2	1.813(10), 1.882(9)
	Cu–Cu	2	2.716(5)	0.0124(5)			2	2.697(2), 2.723(3)
	Cu–Cu	1	3.91(2)	0.0138(5)	8.9(2.2)	0.0078	1	3.826

<sup>a</sup> Fit:  $R$  space,  $3.0 < k < 13.8$ ;  $1.2 < R < 3.0$  ( $N_{\text{imp}} = 14.3$ ) and  $3.5 < R < 4.1$  ( $N_{\text{imp}} = 6.1$ ). <sup>b</sup> Fit:  $R$  space,  $3.0 < k < 13.5$ ;  $1.2 < R < 2.76$  ( $N_{\text{imp}} = 12.4$ ) and  $3.5 < R < 4.05$  ( $N_{\text{imp}} = 5.6$ ). <sup>c</sup> Coordination numbers were kept constant at their model values. <sup>d</sup> Fitted radial distance. <sup>e</sup> Debye–Waller factor. <sup>f</sup> Energy reference shift. <sup>g</sup>  $R$ -factor defined in eq 3. <sup>h</sup> References 17 and 32. <sup>i</sup> The positions of Cu, O, and Si in the core of  $[\text{CuOSi}(\text{O}^+\text{Bu})_3]_4$  are taken to be the same as those for  $[\text{CuOSiPh}(\text{O}^+\text{Bu})_2]_4$  for which the crystal structure is known (ref 17).

imaginary part for the Fourier components of the Cu–Cu and Cu–Si scattering paths. The strong agreement between the experimental results and those of the simulation provides indirect evidence for an accurate choice of the Fermi energy reference ( $E_0$ ).<sup>33</sup> A similar analysis performed for  $[\text{CuO}^+\text{Bu}]_4$  gave agreement in the shape, number of peaks, and phase of the imaginary part, supporting the assignments of nearest neighbor contributions.

The EXAFS fitting results for  $[\text{CuOSi}(\text{O}^+\text{Bu})_3]_4$  and  $[\text{CuO}^+\text{Bu}]_4$  are reported in Table 5. An initial fit was performed by simultaneously varying the coordination number (CN), the radius ( $R$ ), the Debye–Waller factor ( $\sigma^2$ ), and  $E_0$  for each scattering path. Coordination numbers found for each coordination shell of  $[\text{CuOSi}(\text{O}^+\text{Bu})_3]_4$  and  $[\text{CuO}^+\text{Bu}]_4$  were within 0.2–0.4 of the expected values. Therefore, a final fit was performed by setting the CN constant at the known values and then refining  $R$ ,  $\sigma^2$ , and  $E_0$  (Table 5). This approach defines a lower limit for the Debye–Waller factors below which fitting results of actual samples should not be possible.<sup>38</sup> The Cu–O bond distance found for the nearest neighbor O in  $[\text{CuOSi}(\text{O}^+\text{Bu})_3]_4$  is in good agreement with the Cu–O bond distances determined from single-crystal X-ray diffraction (XRD) analysis of  $[\text{CuOSi}$

$(\text{O}^+\text{Bu})_2\text{C}_6\text{H}_5]_4$  (Table 5).<sup>17</sup> The Cu–Cu (adjacent) and Cu–Si distances found for the next-nearest neighbors (2.716(5) and 3.138(1) Å, respectively) fall within the average values for  $[\text{CuOSi}(\text{O}^+\text{Bu})_2\text{C}_6\text{H}_5]_4$  determined from single-crystal XRD data (Table 5).<sup>17</sup> Backscattering from Cu atoms located on the opposite side of the  $[\text{Cu–O}]_4$  ring was found to be the average distance of 3.92(3) Å. This distance is 0.06 Å larger than that determined for  $[\text{CuOSi}(\text{O}^+\text{Bu})_2\text{C}_6\text{H}_5]_4$  by single-crystal XRD, possibly because of the neglect of multiple scattering and Cu–C backscattering contributions. The fitted Cu–O and Cu–Cu distances for  $[\text{CuO}^+\text{Bu}]_4$  are also in good agreement with the values determined from single-crystal XRD characterization of this compound (Table 4).<sup>32</sup>

**EXAFS: As Prepared Samples.** The fitting results for the freshly prepared materials are presented in Table 6. Normalized and atomic background-subtracted  $k^3\chi(k)$  spectra of freshly prepared CuCl/SBA (3.0), CuOSi/SBA (3.5), CuOSi/SBA (5.0), CuO<sup>+</sup>Bu/SBA (3.5), and CuO<sup>+</sup>Bu/SBA (5.0) are shown in Figure 7, parts a–c. The overall signal-to-noise ratio in each spectrum is very good. There is a small glitch at  $6.65 \text{ \AA}^{-1}$  in the spectra of CuOSi/SBA (5.0) and CuCl/SBA (3.0) because of an imperfection in the Si(111) monochromator. The FT  $k^3\chi(k)$  plots



**TABLE 6: Fitting Results for Fresh Samples**

material	shell	CN <sup>a</sup>	<i>R</i> (Å) <sup>b</sup>	$\sigma_2$ (Å <sup>2</sup> ) <sup>c</sup>	<i>E</i> <sub>0</sub> (eV) <sup>d</sup>	<i>R</i> -factor <sup>e</sup>
CuO'Bu/SBA (3.5)	Cu—O	3.6(2)	1.928(4)	0.0041(5)	−1.4(7)	0.0047
	Cu—Cu	2.1(2)	2.87(1)	0.013 <sup>f</sup>		
CuO'Bu/SBA (5.05)	Cu—O	3.4(2)	1.925(4)	0.0055(6)	2.2(8)	0.0056
	Cu—Cu	1.8(2)	2.86(1)	0.013 <sup>f</sup>		
CuOSi/SBA (3.5)	Cu—O	2.4(2)	1.877(8)	0.004(1)	1.5(1.5)	0.0262
	Cu—Si	0.7(7)	3.11(4)	0.006(9)		
CuOSi/SBA (5.0)	Cu—O	2.9(1)	1.895(4)	0.0051(5)	1.9(7)	0.0061
	Cu—Si	1.5(5)	3.12(1)	0.009(4)		
CuCl/SBA (3.0)	Cu—O	2.5(1)	1.904(4)	0.0054(62)	5.2(7)	0.0019
	Cu—Cu	0.4(5)	2.64(3)	0.009(8)		
	Cu—Si	1.0(3)	3.04(2)	0.007(3)		

<sup>a</sup> Coordination number. <sup>b</sup> Fitted radial distance. <sup>c</sup> Debye–Waller factor. <sup>d</sup> Energy reference shift. <sup>e</sup> *R*-factor defined in eq 3. <sup>f</sup> Debye–Waller factor fixed at minimum value established by fit of [CuO'Bu]<sub>4</sub> in Table 4.

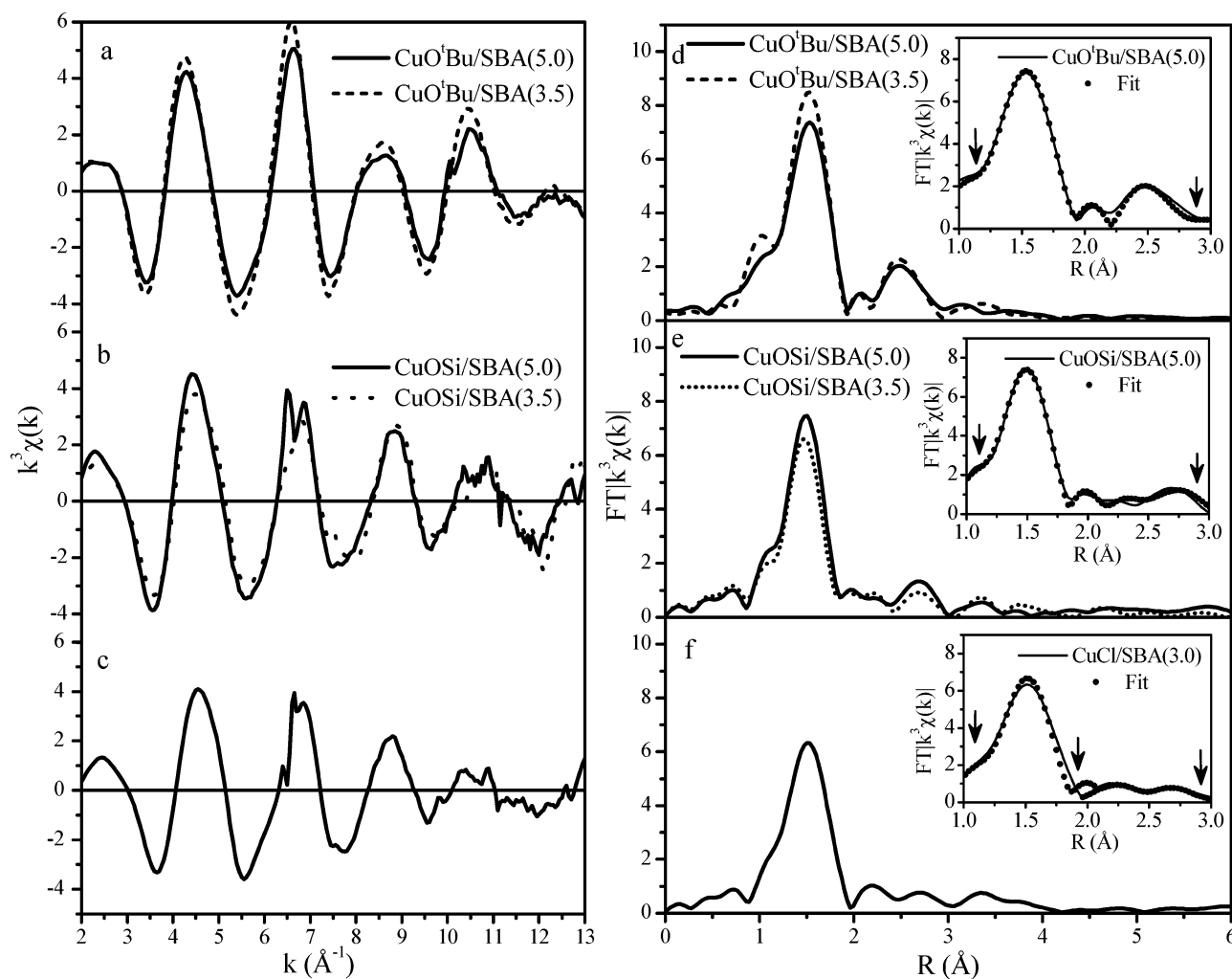


**Figure 7.**  $k^3\chi(k)$  for fresh materials. (a) CuO'Bu/SBA (3.5) and CuO'Bu/SBA (5.0), (b) CuOSi/SBA (3.5) and CuOSi/SBA (5.0), and (c) CuCl/SBA (3.0). Fourier transformed  $k^3\chi(k)$  and the fitting results for fresh materials: (d) CuO'Bu/SBA (3.5) and CuO'Bu/SBA (5.0), (e) CuOSi/SBA (3.5) and CuOSi/SBA (5.0), and (f) CuCl/SBA (3.0). The fits are shown for representative spectra in the insets and are indicated by dots. The fitting region in *r* space is indicated by the arrows.

of the materials are shown in Figure 7, parts d–f, together with representative best fit plots for each material shown as insets. Each spectrum has a prominent Fourier component centered between 1.47 and 1.53 Å, attributed to Cu–O backscattering. The differences in the magnitude of this component are reflected in the values of the fitted CNs (Table 6). Freshly prepared CuCl/SBA (3.0) was found to have an average Cu–O CN of 2.5(1), suggesting that the Cu atoms in this sample are surrounded by two or three oxygen atoms with equal probability. The

average Cu–O CNs found for freshly prepared CuOSi/SBA (3.5) and CuOSi/SBA (5.0) are 2.4(2) and 2.9(1), respectively. In contrast, the average Cu–O CNs found for CuO'Bu/SBA (3.5) and CuO'Bu/SBA (5.0) were noticeably higher (3.6(2) and 3.4(2), respectively), suggesting increased Cu–O interaction, possibly via retention of bridging Cu–O'Bu–Cu linkages.

The interpretation of the Fourier components located at ~2.5 Å was aided by examination of the imaginary part of the FT  $k^3\chi(k)$  plot, as outlined above for the standards. The magni-



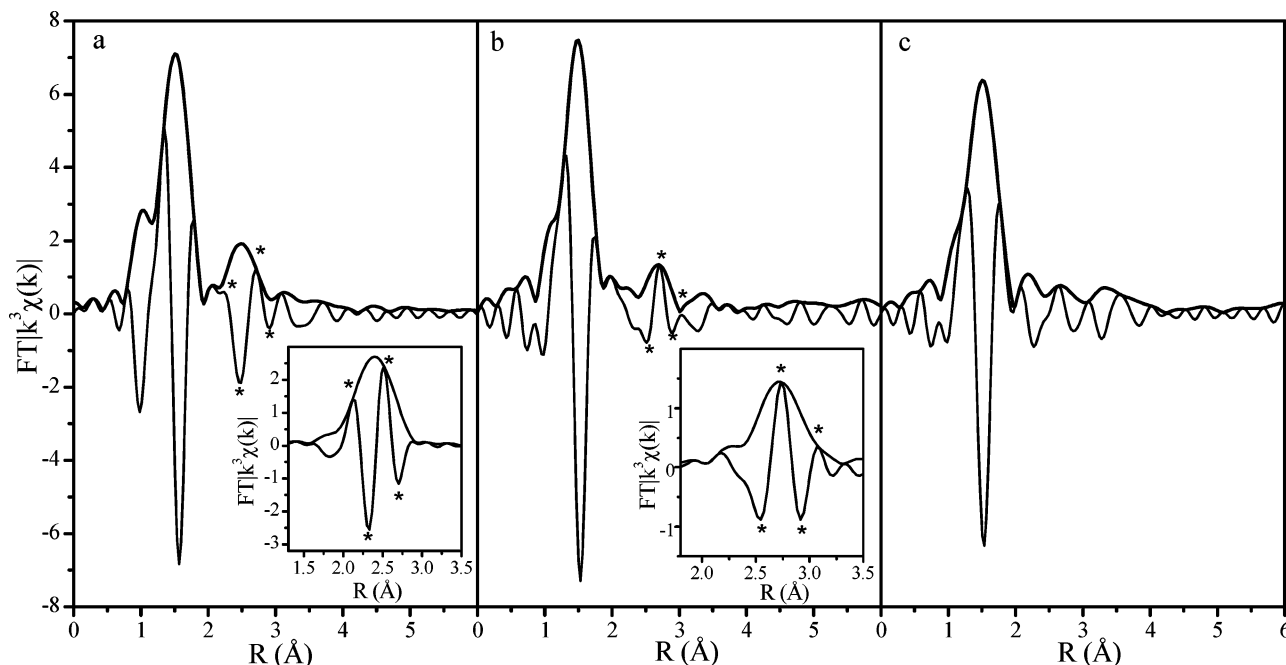


**Figure 8.** Comparison of the shape and number of imaginary peaks of the second shell to the theoretical scattering paths. (a) Magnitude and imaginary parts of CuO'Bu/SBA (5.0) (fresh). Inset is theoretical Cu–Cu scattering modeled using [CuO'Bu]<sub>4</sub>. Similar peak shapes and positions are annotated with the symbol \*. (b) Magnitude and imaginary parts of CuOSi/SBA (5.0) (fresh). Inset is theoretical Cu–Si scattering modeled using [CuOSi(O'Bu)<sub>3</sub>]<sub>4</sub>. Similar peak shapes and positions are annotated with the symbol \*. (c) Magnitude and imaginary parts of the EXAFS spectrum for CuCl/SBA (3.0) (fresh).

**TABLE 7: Comparison of Position of Imaginary Peaks of Fresh Materials to Theoretical Cu–Cu and Cu–Si Scattering Paths for the Peak at 2.2–3.3 Å (Nonphase Corrected)**

peak	$\Delta R^a$				
	CuOSi/SBA (5.0)	CuOtBu/SBA (5.0)	Cu–Cu scattering <sup>b</sup>	Cu–Cu scattering <sup>c</sup>	Cu–Si scattering <sup>c</sup>
1 (positive)		0.25	0.25	0.25	
2 (negative)	0.18	0.03	0.09	0.09	0.18
3 (positive)	0.00	−0.21	−0.09	−0.06	0.00
4 (negative)	−0.18	−0.39	−0.25	−0.21	−0.15
5 (positive)	−0.34				−0.31

<sup>a</sup> Values in table reported as a difference between the position at maximum value of the magnitude of the Fourier transformed data and the position at one of either maximum or minimum in the imaginary parts. <sup>b</sup> Calculated for the structure of [CuO'Bu]<sub>4</sub> at Debye–Waller factors of 0.0 Å<sup>2</sup>. <sup>c</sup> Calculated for the structure of [CuOSi(O'Bu)<sub>3</sub>]<sub>4</sub> at Debye–Waller factors of 0.0 Å<sup>2</sup>.

tude and imaginary parts of the forward FT  $k^3\chi(k)$  plots for freshly prepared CuO'Bu/SBA (3.5) and CuO'Bu/SBA (5.0) are nearly identical. Figure 8a shows the magnitude and imaginary parts of the forward FT  $k^3\chi(k)$  plot for CuO'Bu/SBA (5.0). For comparison, the magnitude and imaginary part of the simulated Cu–Cu backscattering contribution to the FT  $k^3\chi(k)$  for [CuO'Bu]<sub>4</sub> is shown in Figure 8a (inset). The similarity in the shapes and positions of the maxima and minima for the observed and simulated imaginary components suggests that the peak in the FT at 2.5 Å is due to Cu–Cu backscattering. This interpretation is further supported by a consideration of the position of the maxima and minima in the imaginary part of the FT relative to the position of the magnitude of this function, as presented in Table 7.<sup>37a</sup> It is apparent that the agreement between theory and experiment is much closer if the peak at 2.5 Å is attributed primarily to Cu–Cu backscattering rather than Cu–Si backscattering. However, this does not preclude a Cu–Si backscattering contribution of very small magnitude (i.e., from support Si–O–Cu interactions).

The second peaks in the FT  $k^3\chi(k)$  plots for CuO'Bu/SBA (3.5) and CuO'Bu/SBA (5.0), centered at 2.48 Å, were fit assuming Cu–Cu backscattering. Because it is known that a strong correlation exists between  $\sigma^2$  and CN,<sup>38</sup> it was decided to fix  $\sigma^2$  at the value found during the fit of the FT observed for [CuO'Bu]<sub>4</sub>, as shown in Table 5. When the experimental data were fit in this manner, Cu–Cu CN values of 2.1(2) and 1.8(2) were determined for freshly prepared CuO'Bu/SBA (3.5) and CuO'Bu/SBA (5.0), respectively (Table 6). The separation of Cu–Cu nearest neighbors in freshly prepared CuO'Bu/SBA (3.5) (2.87(1) Å) and CuO'Bu/SBA (5.0) (2.86(1) Å) is somewhat longer than that found for [CuO'Bu]<sub>4</sub> (2.716(5) Å), suggesting an increase in the Cu–O–Cu bond angles.

The magnitude and imaginary part of the forward FT  $k^3\chi(k)$  plots for freshly prepared CuOSi/SBA (3.5) and CuOSi/SBA (5.0) are nearly identical. Figure 8b shows the magnitude and imaginary part of the forward FT  $k^3\chi(k)$  plot for CuOSi/SBA (5.0). In this case, the shape and positions of the imaginary part of the peak appearing between 2.2 and 3.3 Å are similar to those obtained for Cu–Si backscattering (Figure 8b, inset). As with the CuO'Bu/SBA samples, this interpretation is also supported by a consideration of the positions of the maxima and minima positions in the imaginary part of the FT relative to the position of the magnitude of this function (see Table 7). Therefore, the dominant next-nearest-neighbor contributions for CuOSi/SBA (3.5) and CuOSi/SBA (5.0) are due to Cu–Si backscattering. No evidence for Cu–Cu next-nearest-neighbor interactions was found. The CNs for Cu–Si backscattering determined from the FT  $k^3\chi(k)$  plots for CuOSi/SBA (3.5) and CuOSi/SBA (5.0) are 0.7(7) and 1.5(5), respectively (Table 6). The large errors associated with these coordination numbers may be indicative of the amorphous nature of the support or a wide variation in Cu–O–Si(O'Bu)<sub>3</sub> bond angles. Interestingly, the Cu–Si scattering distances (3.11(4) and 3.12(1) Å) are statistically identical to the value found by EXAFS for [CuOSi(O'Bu)<sub>3</sub>]<sub>4</sub> (3.138(1) Å) and are similar to related Cu–Si distances in the naturally

occurring Cu silicates shattuckite ( $\text{Cu}_5(\text{SiO}_3)_4(\text{OH})_2$ ) (3.111 Å),<sup>39</sup> diopside ( $\text{Cu}_6[\text{Si}_6\text{O}_{18}]$ ) (3.089 Å),<sup>40</sup> and planchéite ( $\text{Cu}_8(\text{Si}_4\text{O}_{11})_2(\text{OH})_4 \cdot x\text{H}_2\text{O}$ ) (3.138 Å).<sup>39</sup>

The magnitude and imaginary parts of the forward FT  $k^3\chi(k)$  plot for freshly prepared CuCl/SBA (3.0) are shown in Figure 8c. The major peak at 2.7 Å matches closely with the position of the second Fourier component in the nonphase corrected EXAFS spectra of CuOSi/SBA (3.5) and CuOSi/SBA (5.0) and is, therefore, assumed to be due to Cu–Si backscattering. The first (relatively weak) peak at 2.23 Å was determined to be a real Fourier component by examining the effect of the window function used. In terms of position, it best matches the Cu–Cu scattering of Cu foil or Cu–Cl scattering from CuCl (Figure 4). Because the peak was not well isolated, identification by analysis of the imaginary part was not attempted.

The fitting of the FT  $k^3\chi(k)$  for CuCl/SBA (3.0) was done over two ranges. The first, 1.2–1.9 Å, being attributed to Cu–O backscattering and the second, 1.9–2.9 Å, due to Cu–Cu and Cu–Si backscattering. As noted in Table 6, the best fit for the second region results in a Cu–Cu distance of 2.64(3) Å. This distance is larger than the Cu–Cu distance for both  $\text{Cu}_n$  clusters ( $n = 2-5$ ) (2.22–2.4 Å)<sup>41</sup> and bulk Cu metal (2.54 Å). The fitted Cu–Cu distance may, therefore, be indicative of Cu atoms situated not far from each other but not strongly bonded into a cluster. The low CN for Cu (0.4(5)) also suggests that the Cu atoms in freshly prepared CuCl/SBA (3.0) are well isolated, mostly as  $\equiv\text{Si}-\text{O}-\text{Cu}$ . Quantum chemical calculations by Lopez et al. predict that such species are stable.<sup>42</sup>

**Thermal Treatments in He.** As noted earlier, the materials prepared via grafting of  $[\text{CuO}^i\text{Bu}]_4$  and  $[\text{CuOSi}(\text{O}^i\text{Bu})_3]_4$  on SBA-15 were heated in He at 573 K for 1 h to remove the organic ligands via elimination of  $\text{CH}_2\text{C}(\text{CH}_3)_2$  and  $\text{H}_2\text{O}$ . The loss of organic ligands was confirmed by EA, TGA, IR spectroscopy, and  $^1\text{H}$  NMR spectroscopy. The FT  $k^3\chi(k)$  spectra of CuO<sup>i</sup>Bu/SBA (3.5), CuO<sup>i</sup>Bu/SBA (5.0), CuOSi/SBA (3.5), CuOSi/SBA (5.0), and CuCl/SBA (3.0) are shown in Figure 9. The FT  $k^3\chi(k)$  spectra for both CuO<sup>i</sup>Bu/SBA (3.5) and CuO<sup>i</sup>Bu/SBA (5.0) (Figure 9a, inset) have spectral characteristics very similar to those seen in the spectrum of Cu foil (Figure 5b). The peaks at 2.23, 3.4, 4.1, and 4.7 Å (nonphase corrected) are attributable to the first four coordination shells of Cu in Cu metal. This, coupled with the absence of any significant Fourier component that can be assigned to Cu–O backscattering, suggests that all detectable Cu has been reduced to Cu metal. In contrast, the FT  $k^3\chi(k)$  spectra of CuOSi/SBA (3.5) and CuOSi/SBA (5.0) after He treatment at 573 K for 1 h (Figure 9b, inset) show a prominent Fourier component at 1.47 Å assigned to Cu–O backscattering, suggesting that the dominant sites are still  $\text{Cu}^{\text{I}}$  cations associated with O. The spectra of CuOSi/SBA (3.5) and CuOSi/SBA (5.0) also exhibit peaks at 2.11, 3.34, 4.1, and 4.7 Å, but they are significantly smaller in magnitude than those observed in the spectra of CuO<sup>i</sup>Bu/SBA (3.5) and CuO<sup>i</sup>Bu/SBA (5.0), suggesting the presence of only minor amounts of Cu metal. The FT  $k^3\chi(k)$  spectrum of CuCl/SBA (3.0) after He treatment at 573 K for 1 h (Figure 9c) is quite similar to those of CuOSi/SBA (3.5) and CuOSi/SBA (5.0), suggesting that most sites are  $\text{Cu}^{\text{I}}$  cations with associated O atoms and that only a small fraction of Cu is in a metallic state. The small peak at 2.63 Å in the FT  $k^3\chi(k)$  plot of CuCl/SBA (3.0) could not be assigned definitively.

The first two Fourier components characteristic of supported Cu particles in He treated CuO<sup>i</sup>Bu/SBA (3.5) and CuO<sup>i</sup>Bu/SBA (5.0) were fitted using three different Cu–Cu scattering contributions. A single Cu–Cu scattering contribution was used

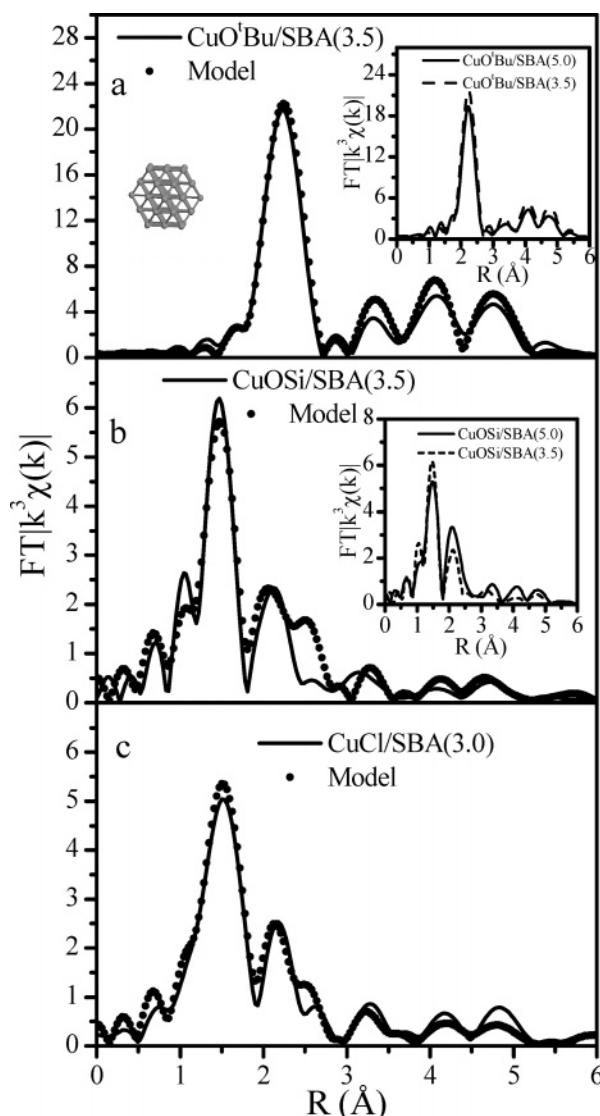


**Figure 9.** Fourier transformed  $k^3\chi(k)$  and model comparison results for materials after treatment in He (573 K for 1 h). (a) Comparison between a 55-atom copper particle model (cluster shown in inset) and CuO<sup>i</sup>Bu/SBA (3.5) after He treatment at 573 K. FEFF model calculated assuming  $S_0^2 = 0.86$  and  $\sigma^2 = 0.0072 \text{ \AA}^2$  for all scattering paths. Inset is a comparison between CuO<sup>i</sup>Bu/SBA (3.5) and CuO<sup>i</sup>Bu/SBA (5.0). (b) Comparison between CuOSi/SBA (3.5) after helium treatment at 573 K and a model which represents a linear combination of CuOSi/SBA (3.5) (fresh) and CuO<sup>i</sup>Bu/SBA (3.5) (He 573 K). Inset is a comparison between CuOSi/SBA (3.5) and CuOSi/SBA (5.0). (c) Comparison between CuCl/SBA (3.0) after helium treatment at 573 K and a model which represents a linear combination of CuCl/SBA (3.0) (fresh) and CuO<sup>i</sup>Bu/SBA (3.5) (He 573 K).

for the first shell, whereas both a single Cu–Cu scattering contribution and a relevant multiscattering path (focusing,<sup>33a</sup> MS1) were included in the fit of the second shell. The total number of radial distances used in the fit could be reduced by two by recognizing that the scattering path lengths,  $R_{\text{CuCu}_j}$ , are each related to a single cluster lattice parameter, which is known to vary with cluster sizes and temperatures.<sup>43</sup> Therefore, the isotropic lattice expansion factor,  $\epsilon$ , can be introduced as shown in eq 3. In this equation,  $R_{\text{CuCu}_j|\text{known}}$  is the distance separating the absorbing and backscattering Cu atoms predicted on the basis of the lattice parameter chosen for the Cu foil FEFF simulation (3.61 Å at 298 K).  $R_{\text{CuCu}_j|\text{exp}}$  is the distance separating the absorbing and backscattering Cu atoms in the He treated CuO<sup>i</sup>Bu/SBA (3.5) and CuO<sup>i</sup>Bu/SBA (5.0). Single values of  $\epsilon$  and  $E_0$  were optimized to model all paths in the fit, whereas

**TABLE 8: Fitting Results for Samples after Helium Treatment at 573 K for 1 h**

material	shell	CN <sup>a</sup>	R (Å) <sup>b</sup>	σ <sup>2</sup> (Å <sup>2</sup> ) <sup>c</sup>	E <sub>0</sub> (eV) <sup>d</sup>	R-factor <sup>e</sup>
CuO'Bu/SBA (3.5)	Cu—Cu	7.8(3)	2.52(2)	0.0062(9)	3.0(5)	0.0025
	Cu—Cu	4.7(2.6)	3.57(2)	0.012(4)		
	MS1 <sup>f</sup>	22(16)	3.79(2)	0.01 <sup>g</sup>		
CuO'Bu/SBA (5.0)	Cu—Cu	7.6(3)	2.52(1)	0.0072(3)	1.5(6)	0.0021
	Cu—Cu	4.2(2.9)	3.58(1)	0.013(5)		
	MS1 <sup>f</sup>	18(14)	3.80(1)	0.01 <sup>g</sup>		
CuOSi/SBA (3.5)	Cu—O	1.9(3)	1.85(1)	0.003(1)	0.3(2.4)	0.0261
	Cu—Cu	0.7(6)	2.55(2)	0.007(5)		
CuOSi/SBA (5.0)	Cu—O	1.7(1)	1.851(6)	0.0029(7)	1.4(1.3)	0.0249
	Cu—Cu	1.2(3)	2.54(1)	0.007(1)		
	Cu—Cu	0.9(9)	3.59(1)	0.009(7)		
CuCl/SBA (3.0)	Cu—O	2.38(2)	1.902(9)	0.006(1)	6.7(1.4)	0.0101
	Cu—Cu	0.5(3)	2.58(1)	0.004(3)		

<sup>a</sup> Coordination number. <sup>b</sup> Fitted radial distance assuming isotropic lattice expansion α. <sup>c</sup> Debye–Waller factor. <sup>d</sup> Energy reference shift. <sup>e</sup> R-factor defined in eqn. 3. <sup>f</sup> Fixed value. <sup>g</sup> This is the first significant multiscattering path. The radial distance determined for MS1 is half the total path length scattering distance.

CN and σ<sup>2</sup> were refined independently for each path, except MS1. A value of 0.01 Å<sup>2</sup> was set for σ<sup>2</sup> of MS1 based on prior knowledge of values found in the fitting of the Cu foil (not discussed). This procedure is identical to that used for analysis of EXAFS data for carbon-supported Pt nanoparticles.<sup>44</sup>

$$R_{\text{CuCu}}|_{\text{exp}} = (\epsilon + 1)R_{\text{CuCu}}|_{\text{known}} \quad (3)$$

The results for He treated CuO'Bu/SBA (3.5) and CuO'Bu/SBA (5.0) of the fitting procedure described above are shown in Table 8. The ratio of average CNs for the first and second shell is consistent with that reported for a 55-atom face-centered cubic (fcc) cluster.<sup>41</sup> To test this conclusion, a complete FEFF simulation was performed to determine the expected average scattering of a single Cu atom in a 55-atom fcc cuboctahedron.<sup>41</sup> The simulation was carried out assuming  $S_0^2 = 0.86$  and  $\sigma^2 = 0.0072$  Å<sup>2</sup> (the Debye–Waller factor used to fit the first shell of metallic Cu (Table 8)). The resulting fit to the FT  $k^3\chi(k)$  plot of CuO'Bu/SBA (3.5) is shown in Figure 9a. Close agreement between experiment and the model is seen for the first coordination shell. Although the positions of peaks for the simulated FT coincide with those observed experimentally, the intensities of the simulated peaks are somewhat larger. This is probably due to the use of a single value of the Debye–Waller factor for all shells. The close agreement between simulation and experiment seen for both CuO'Bu/SBA (3.5) and CuO'Bu/SBA (5.0) indicates that upon He pretreatment the Cu atoms in freshly prepared grafted materials are reduced and sinter to form crystalline Cu particles with an average diameter of ca. 7 Å. Transmission electron microscopy (TEM) was used in an attempt to observe the particle size distribution; however, reliable size distributions could not be obtained because of severe beam damage, as evidenced by rapid formation of large Cu particles.

A similar methodology to that described above was used to analyze the Cu metal species observed in He treated (573 K) CuOSi/SBA (3.5) and CuOSi/SBA (5.0). The CNs obtained for the first two Cu—Cu shells were not consistent with those expected for metal nanoparticles. Consequently, a linear combination of the experimental data for He treated (573 K) CuO'Bu/SBA(3.5) with freshly prepared CuOSi/SBA (3.5) or CuOSi/SBA (5.0) was used as a model for  $k^3\chi(k)$  and FT  $k^3\chi(k)$  plots of He-treated (573 K) CuOSi/SBA (3.5) or CuOSi/SBA (5.0). The rationale for this model is that He-treated CuOSi/SBA (3.5) and CuOSi/SBA (5.0) contain a mixture of isolated Cu<sup>I</sup> species and Cu nanoparticles. The fit of the model to the data for CuOSi/SBA (3.5) is shown in Figure 9b. On the basis

**TABLE 9: Linear Combination Fitting Results**

material	$x_{\text{fresh}}^a$	$x_{\text{metal}}^b$	% Cu available for catalysis <sup>c</sup>
CuO'Bu/SBA (3.5)	0.000	1.000	58.1
CuO'Bu/SBA (5.0)	0.000	1.000	58.1
CuOSi/SBA (3.5)	0.880	0.120	94.9
CuOSi/SBA (5.0)	0.785	0.215	91.0
CuCl/SBA (3.0)	0.893	0.107	95.5

<sup>a</sup> Fraction of each respective fresh samples. <sup>b</sup> Fraction of experimental CuO'Bu/SBA(5.0) after He treatment assuming 55 atom cluster (fcc cluster with corners removed). <sup>c</sup> Accounts for metal fraction in fit by counting only the fraction of surface atoms in a 55 atom fcc cluster with corners removed.

of this approach, the fraction of Cu present as isolated Cu<sup>I</sup> centers was determined to be 88.0% for CuOSi/SBA (3.5) and 78.5% for CuOSi/SBA (5.0) (Table 9).

The Cu—O CNs for He-treated (573 K) CuOSi/SBA (3.5) (1.9(3)) and CuOSi/SBA (5.0) (1.7(1)) decreased by about 1 relative to the values for these materials determined prior to pretreatment. The decrease in the Cu—O CN is likely due to a loss of O atoms occurring during the decomposition of the organic ligands, as well as a decrease in the fraction of atomically dispersed Cu because of reduction and sintering to form Cu crystallites.

EXAFS fitting results for He-treated (573 K) CuCl/SBA (3.0) show only a small loss in Cu—O CN compared to the freshly prepared material, with no appreciable change in the average Cu—O bond distance, suggesting little change in the Cu species upon He treatment of these samples. The Cu—Cu coordination remained the same (within error); however, the fitted average Cu—Cu bond distance (2.58(1) Å) is in much closer agreement to that expected in Cu metal (2.55 Å). A linear combination of the experimental data for He-treated (573 K) CuO'Bu/SBA (3.5) with freshly prepared CuCl/SBA (3.0) was used as a model for  $k^3\chi(k)$  and FT  $k^3\chi(k)$  plots of He-treated (573 K) CuCl/SBA (3.0). Figure 9c shows that the experimental data are well-represented by a model in which 89% of the Cu is present as isolated Cu<sup>I</sup> species (Table 9).

The preceding discussion shows that the state of Cu after He pretreatment at 573 K is a strong function of the copper precursor used. Grafting of [CuO'Bu]<sub>4</sub> results in the agglomeration of all the Cu into ca. 7 Å diameter crystallites of metallic Cu. However, grafting of either [CuOSi(O'Bu)<sub>3</sub>]<sub>4</sub> or CuCl produces materials in which 80–90% of the Cu is atomically dispersed.



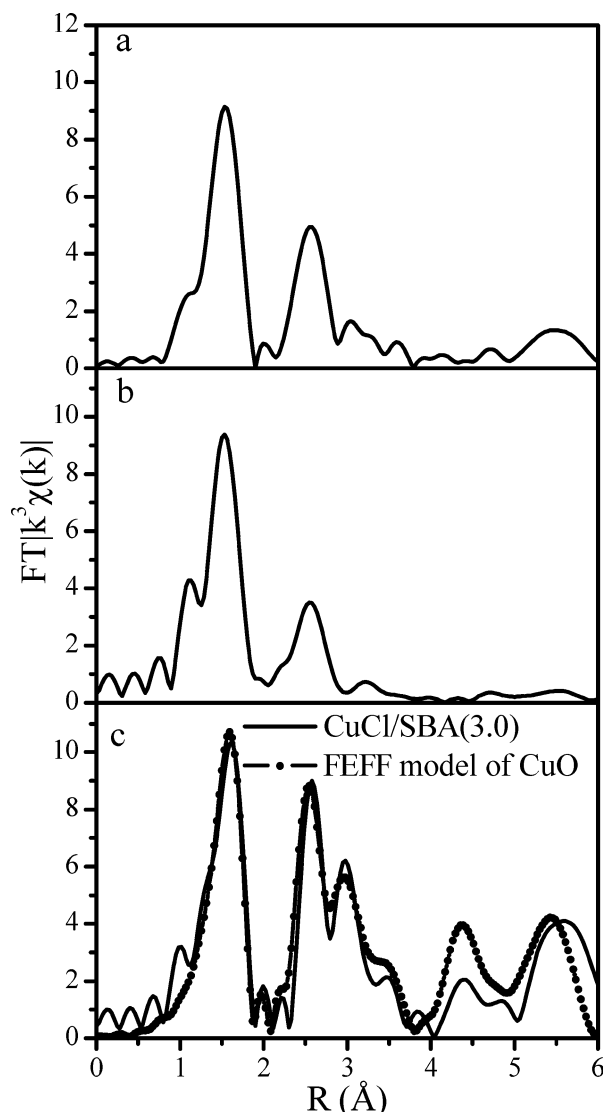


**Figure 10.** Fourier transformed  $k^3\chi(k)$  spectra of samples after  $O_2$  treatment at 773 K for 1 h: (a) CuO'Bu/SBA (5.0), (b) CuOSi/SBA (5.0), (c) CuCl/SBA (3.0) together with FEFF model of CuO. The model consists of one Cu–O shell centered at 1.62 Å and Cu–Cu scattering for all subsequent shells. CNs of all shells were set at their crystallographic numbers. The Debye–Waller factor was the only adjusted model parameter, set at 0.004 Å<sup>2</sup> for Cu–O and 0.007 Å<sup>2</sup> for Cu–Cu scattering in all subsequent shells.

**Oxygen Treatment at 773 K.** The nonphase corrected FT  $k^3\chi(k)$  spectra of CuCl/SBA (3.0), CuOSi/SBA (5.0), and CuO'Bu/SBA (5.0) taken after  $O_2$  treatment at 773 K for 1 h are shown in Figure 10. The appearance of the Fourier transform for CuCl/SBA (3.0) agrees closely with that of CuO (Figure 5b), which suggests that upon oxidation at 773 K all of the Cu in CuCl/SBA (3.0) is converted into particles of ordered CuO. This is further supported by comparing the FT  $k^3\chi(k)$  spectra of CuCl/SBA (3.0) to a FEFF model of CuO. The model is shown in Figure 10c and consists of the following scattering paths: Cu–O (equatorial, CN = 4,  $R = 1.95\text{--}1.96$  Å), (Cu–Cu)<sub>1</sub> (CN = 4,  $R = 2.90$  Å), (Cu–Cu)<sub>2</sub> (CN = 4,  $R = 3.08$  Å), (Cu–Cu)<sub>3</sub> (CN = 2,  $R = 3.17$  Å), (Cu–Cu)<sub>4</sub> (CN = 2,  $R = 3.42$  Å), (Cu–Cu)<sub>5</sub> (CN = 2,  $R = 3.75$  Å), (Cu–Cu)<sub>6</sub> (CN = 4,  $R = 4.67$  Å), (Cu–Cu)<sub>7</sub> (CN = 4,  $R = 5.2406$  Å), and multiscattering Cu–Cu paths at distances above 5 Å. The Debye–Waller factor was the only adjustable parameter, and it was set to 0.004 Å<sup>2</sup> for Cu–O and 0.007 Å<sup>2</sup> for Cu–Cu scattering in all subsequent shells. By use of the model as a

basis for peak identification, the positions of the Fourier components were assigned in the following manner: 1.62 Å (nonphase corrected) Cu–O (equatorial); 2.54 Å (nonphase corrected) (Cu–Cu)<sub>1</sub> and (Cu–Cu)<sub>2</sub>; 2.97 Å (nonphase corrected) to (Cu–Cu)<sub>2</sub>, (Cu–Cu)<sub>3</sub>, and (Cu–Cu)<sub>4</sub>; 3.46 Å (nonphase corrected) to (Cu–Cu)<sub>4</sub> and (Cu–Cu)<sub>5</sub>; and 4.35 Å and 5.52 Å to Cu–Cu single and multiple scattering contributions.

The FT  $k^3\chi(k)$  plot for CuO'Bu/SBA (5.0) contains all of the Fourier components observed in the spectrum for CuCl/SBA (3.0) except that the features appearing above 3.0 Å are less intense and broader. This indicates that small CuO domains were formed as a result of oxidation of the 7-Å Cu particles formed after He treatment at 573 K. The FT  $k^3\chi(k)$  plot for CuOSi/SBA (5.0) after  $O_2$  treatment has a prominent Fourier component at 1.62 Å and a less intense peak at 2.97 Å but does not show features beyond 3.0 Å because of long-range order in CuO. The results shown in Figure 10 suggest that irrespective of the Cu precursor,  $O_2$  oxidation of the He-treated samples for 1 h at 773 K results in the conversion of the supported Cu into CuO. This conclusion is supported by the XANES data presented in Figure 4 and Table 4, which show that after oxidation all detected Cu is formally Cu<sup>II</sup>. However, the dispersion and ordering of these domains depend strongly on the composition of the Cu precursor.

On the basis of the preceding discussion, the first two or three shells of each sample were fit using theoretical phase and amplitude functions for Cu–O and Cu–Cu backscattering appropriate for CuO (Table 10). The CN for the first shell in each spectrum, corresponding to Cu–O backscattering, is  $\sim 4$  (Table 10), which is consistent with that expected for the four equatorial O atoms surrounding each Cu atom in CuO. The fitted Cu–O distance range from 1.947 to 1.934 Å agrees reasonably well with the Cu–O distance for bulk CuO (1.95 and 1.96 Å). The contribution because of scattering from the axial O atoms could not be fitted because of the large Debye–Waller factor associated with these atoms, resulting from Jahn–Teller distortion.<sup>45</sup> Clear differences in the state of dispersion of CuO can be discerned from CNs for the second Fourier component in each spectrum (Table 10). As mentioned in the discussion of the FEFF simulation, this Fourier component has two Cu–Cu backscattering contributions (Cu–Cu)<sub>1</sub> (CN = 4,  $R = 2.90$  Å) and (Cu–Cu)<sub>2</sub> (CN = 4,  $R = 3.08$  Å). The CN for the second Fourier component of CuCl/SBA (3.0) is 6.1(1.6), which is smaller than that for CuOSi/SBA (5.0), 5.1(1.2), and CuO'Bu/SBA (5.0), 4.3(1.2). These results indicate that the dispersion of CuO increases in the order CuO'Bu/SBA (5.0)  $\approx$  CuOSi/SBA (5.0) < CuCl/SBA (3.0).

The formation of significantly larger domains of CuO upon oxidation of CuCl/SBA (3.0), as compared to CuO'Bu/SBA (5.0) or CuOSi/SBA (5.0), is difficult to explain. A possible interpretation is that the agglomeration of CuO is facilitated by Cl atoms retained from the initial sample preparation. Previous studies have shown that chlorosilane species form under anhydrous conditions upon treatment of silica with CuCl at temperatures above 673 K.<sup>46</sup> Because CuCl/SBA (3.0) was prepared by heating SBA-15 in the presence of CuCl at 893 K, some Si–Cl linkages were likely formed. It is possible that during oxidation at 573 K some of the Si–Cl groups reacted with adjacent Si–OH groups to release HCl and form siloxane bridges (reaction 1). The gaseous HCl could then react with Cu–O–Si species to form a silanol group and gaseous CuCl (reaction 2). Subsequent oxidation of CuCl vapor would lead to formation of CuO crystallites (reaction 3). Although this

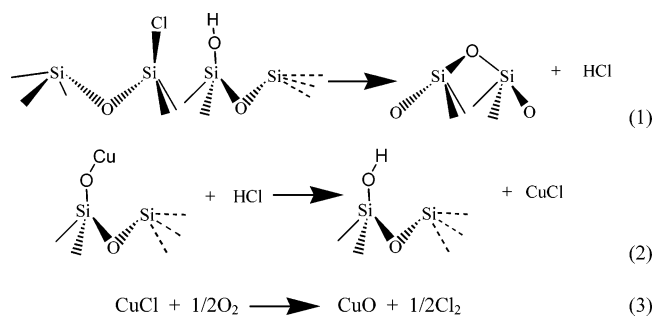


TABLE 10: Fitting Results for Samples after O<sub>2</sub> Treatment at 773K for 1 h

material	shell	CN <sup>a</sup>	R (Å) <sup>b</sup>	σ <sup>2</sup> (Å <sup>2</sup> ) <sup>c</sup>	E <sub>0</sub> (eV) <sup>d</sup>	R-factor <sup>e</sup>
CuO'Bu/SBA (5.0)	Cu—O	4.2(2)	1.939(4)	0.0047(4)	−1.5(8)	0.0031
	Cu—Cu	4.3(1.4)	2.92(1)	0.007(3)	4.9(2.6)	
	Cu—Cu	2.3(2.3)	3.12(3)	0.006(6)		
CuOSi/SBA (5.0)	Cu—O	4.0(2)	1.934(3)	0.0050(4)	−0.4(6)	0.0044
	Cu—Cu	5.1(1.2)	2.883(8)	0.017(2)		
CuCl/SBA (3.0)	Cu—O	4.4(3)	1.947(5)	0.0050(6)	1.6(1.1)	0.0034
	Cu—Cu	6.1(1.6)	2.94(1)	0.007(3)	7.8(2.1)	
	Cu—Cu	3.6(1.8)	3.14(1)	0.003(2)		

<sup>a</sup> Coordination number. <sup>b</sup> Fitted radial distance. <sup>c</sup> Debye–Waller factor. <sup>d</sup> Energy reference shift. <sup>e</sup> R-factor defined in eq 3.

sequence of reactions has not been previously reported, the reverse process is known to occur during the redispersion of agglomerated metal oxide and metallic clusters of Pt and Ir.<sup>47</sup>



## Conclusions

EXAFS, in combination with XANES, was used to characterize the local environment of Cu supported on SBA-15 mesoporous silica. Analysis of the EXAFS data was aided by the use of standards, and in particular [CuOSi(O'Bu)<sub>3</sub>]<sub>4</sub>, which serves as a model for Cu—O—Si bonding. Simulated EXAFS spectra, based on proposed models, were used to identify the origin of the peaks appearing in the Fourier transform of the EXAFS scattering function,  $k^3\chi(k)$ . Identification of the atoms from which backscattering occurred was further aided by analysis of the imaginary part of the nonphase corrected FT  $k^3\chi(k)$ .

The local environments of as prepared samples of Cu supported on SBA-15 prepared from [CuO'Bu]<sub>4</sub>, [CuOSi(O'Bu)<sub>3</sub>]<sub>4</sub>, and CuCl are quite similar. In all cases, Cu is present as Cu<sup>I</sup>, largely as isolated cations. Evidence for Cu—Cu backscattering is seen in the case of samples prepared from [CuO'Bu]<sub>4</sub>, and Cu—Si backscattering is seen in the case of samples prepared from [CuOSi(O'Bu)<sub>3</sub>]<sub>4</sub>, indicating that the latter precursor leads to better isolation of the dispersed Cu. When CuCl is used as the precursor, there is evidence for Cu—Si backscattering and a small contribution due to Cu—Cu backscattering. The effects of precursor composition become clearly evident upon sample treatment in He at 773 K. The sample prepared using [CuO'Bu]<sub>4</sub> as the precursor undergoes complete loss of the organic ligands and reduction of Cu<sup>I</sup> to metallic Cu<sup>0</sup>. Detailed analysis of the EXAFS data for this sample indicates that the Cu is present as crystallites roughly 7 Å in diameter. By strong contrast, the Cu in the sample prepared from [CuOSi(O'Bu)<sub>3</sub>]<sub>4</sub> remains largely as isolated Cu<sup>I</sup> cations (80–90%), and only a small fraction forms crystallites of Cu metal (20–10%). A high fraction of atomically dispersed Cu (90%) is also retained in the thermally treated sample prepared from CuCl. Upon being heated in O<sub>2</sub> at 773 K, the Cu in all of the samples is oxidized to the Cu<sup>II</sup> state and the EXAFS data show clear evidence for the formation of CuO. In the case of the samples prepared from CuCl, the data suggest that well-

defined crystallites of CuO are formed. The formation of these particles is facilitated by the release of HCl from Si—Cl species present on the surface of the support produced during the high-temperature reaction of CuCl with silanol groups on the surface of SBA-15. Evidence for CuO is also present in the samples prepared from [CuO'Bu]<sub>4</sub>, but in this case the crystallites appear to be very small and amorphous. In contrast, only highly dispersed CuO species, lacking any long-range order, are formed upon oxidation of the sample prepared from [CuOSi(O'Bu)<sub>3</sub>]<sub>4</sub>.

**Acknowledgment.** The authors thank the EXAFS experimental team (Dr. S. H. Choi, J. Bronkema, Dr. S. Mukhopadhyay, N. Stephenson, B. Wood, Q. T. Liu, M. Zerella, and Andreas Hyden) for their assistance in collecting data at SSRL and NSLS. We also thank A. Frenkel for insightful discussions concerning the analysis of metal clusters. Last, we thank support staff at BL 6.2 of SSRL and BL X-11A of NSLS and in particular K. Pandya (NSLS) for useful discussions. Portions of this research were carried out at the Stanford Synchrotron Radiation Laboratory, a national user facility operated by Stanford University on behalf of the U.S. Department of Energy, Office of Basic Energy Sciences. Research carried out at the National Synchrotron Light Source, Brookhaven National Laboratory, is supported by the U.S. Department of Energy, Division of Materials Sciences and Division of Chemical Sciences, under Contract No. DE-AC02-98CH10886. This work was supported by the Methane Conversion Cooperative funded by BP and by the Department of Energy, under Contract No. DE-AC03-76SF00098.

## References and Notes

- (1) (a) Fisher, I. A.; Bell, A. T. *J. Catal.* **1997**, *172*, 222. (b) Meitzner, G.; Iglesia, E. *Catal. Today* **1999**, *53*, 433. (c) Kau, L.-S.; Hodgson, K. O.; Solomon, E. I. *J. Am. Chem. Soc.* **1989**, *111*, 7103.
- (2) (a) Iwanoto, M.; Yokoo, S.; Sakai, K.; Kawaga, S. *J. Chem. Soc., Faraday Trans.* **1981**, *177*, 1629. (b) Sato, S.; Iijima, M.; Nakayama, T.; Sodesawa, T.; Nozaki, F. *J. Catal.* **1997**, *169*, 447.
- (3) (a) Anderson, S. A.; Root, T. W. *J. Catal.* **2003**, *217*, 396. (b) King, S. T. *J. Catal.* **1996**, *161*, 530.
- (4) (a) Groothaert, M. H.; van Bokhoven, J. A.; Battiston, A. A.; Weckhuysen, B. M.; Schoonheydt, R. A. *J. Am. Chem. Soc.* **2003**, *125*, 7629–7640. (b) Costa, P. D.; Moden, B.; Meitzner, G. D.; Lee, D. K.; Iglesia, E. *Phys. Chem. Chem. Phys.* **2002**, *4*, 4590–4601. (c) Iwamoto, M.; Yahiro, H.; Yu-u, Y.; Shundo, S.; Mizuno, N. *Shokubai* **1990**, *32*, 430.
- (5) (a) Günter, M. M.; Ressler, T.; Jentoft, R. E.; Bems, B. *J. Catal.* **2001**, *203*, 133. (b) Kniep, B. L.; Ressler, T.; Rabis, A.; Girgsdies, F.; Baenitz, M.; Steglich, F.; Schlögl, R. *Angew. Chem., Int. Ed.* **2004**, *43*, 2004. (c) Geus, J. W.; van Dillen, A. J., In *Preparation of Solid Catalysts*; Ertl, G.; Knozinger, H.; Weitkamp, J., Eds.; Wiley-VCH: Weinheim, Germany, 1999; p 460 (Review of deposition–precipitation).
- (6) (a) Spencer, M. S. *Nature* **1986**, *323*, 685.
- (7) (a) Bell, A. T. *Science* **2003**, *299*, 1688. (b) Arakawa, H.; Aresta, M.; Armor, J. N.; Barteau, M. A.; Beckman, E. J.; Bell, A. T.; Bercaw, J. E.; Creutz, C.; Dinjus, E.; Dixon, D. A.; Domen, K.; DuBois, D. L.; Eckert, J.; Fujita, E.; Gibson, D. H.; Goddard, W. A.; Goodman, D. W.; Keller, J.; Kubas, G. J.; Kung, H. H.; Lyons, J. E.; Manzer, L. E.; Marks, T. J.; Morokuma, K.; Nicholas, K. M.; Periana, R.; Que Jr., J.; Rostrup-Nielson, J.; Sachtler, W. H. M.; Schmidt, L. D.; Sen, A.; Somorjai, G. A.; Stair, P. C.;

- Stults, B. R.; Tumas, W. *Chem. Rev.* **2001**, *101*, 953. (c) Kanai, Y.; Watanabe, T.; Fujitani, T.; Saito, M.; Nakamura, J.; Uchijama, T. *Catal. Lett.* **1994**, *27*, 67.
- (8) Drake, I.; Fudjald, K. F.; Tilley, T. D.; Bell, A. T. *J. Catal.*, in press.
- (9) (a) Fudjald, K. L.; Tilley, T. D. *J. Catal.* **2003**, *216*, 265. (b) Tilley, T. D. *J. Mol. Catal. A: Chem.* **2002**, *182–183*, 17. (c) De Vos, D. E.; Dams, M.; Sels, B. F.; Jacobs, P. A. *Chem. Rev.* **2002**, *102*, 3615–3640. (d) Thomas, J. M. *Top. Catal.* **2001**, *15*, 85. (e) Grasselli, R. K. *Top. Catal.* **2001**, *15*, 93. (f) Basset, J.-M.; Lefebvre, F.; Santini, C. *Coord. Chem. Rev.* **1998**, *178*, 1703. (g) Scott, S. L.; Basset, J.-M. *J. Mol. Catal.* **1994**, *86*, 5. (h) Che, M.; Bonnevot, L. *Successful Design of Catalysts*; Elsevier: Amsterdam, 1988; pp 147–158. (i) Dyrek, K.; Che, M. *Chem. Rev.* **1997**, *97*, 305–331. (j) Hegedus, L. L.; Avis, R.; Bell, A. T.; Boudart, M.; Chen, N. Y.; Gates, B. T.; Haag, W. O.; Somorjai, G. A.; Wei, J. *Catalyst Design: Progress and Perspectives*; Wiley: New York, 1987.
- (10) (a) Jarupatrakorn, J.; Tilley, T. D. *J. Am. Chem. Soc.* **2002**, *124*, 8380. (b) Coles, M. P.; Lugmair, C. G.; Terry, K. W.; Tilley, T. D. *Chem. Mater.* **2000**, *12*, 122. (c) Sheldon, R. A.; Wallau, M.; Arends, I. W. C. E.; Schuchardt, U. *Acc. Chem. Res.* **1998**, *31*, 485. (d) Murugavel, R.; Roesky, H. W. *Angew. Chem., Int. Ed. Engl.* **1997**, *36*, 477. (e) Notari, B. *Adv. Catal.* **1996**, *41*, 253. (f) Corma, A.; Esteve, P.; Martínez, A.; Valencia, S. *J. Catal.* **1995**, *152*, 18. (g) Maschmeyer, T.; Rey, F.; Sanker, G.; Thomas, J. M. *Nature* **1995**, *378*, 159. (h) Khouw, C. B.; Dartt, C. B.; Labinger, J. A.; Davis, M. E. *J. Catal.* **1994**, *149*, 195. (i) Tanev, P. T.; Chibwe, M.; Pinnavaia, T. J. *Nature* **1994**, *368*, 321. (j) Clerici, M. G. *Appl. Catal.* **1991**, *62*, 249.
- (11) (a) Vidal, V.; Théolier, A.; Thivole-Cazat, J.; Basset, J. M.; Corker, J. J. *Am. Chem. Soc.* **1996**, *118*, 4595 and references therein. (b) Vidal, V.; Théolier, A.; Thivole-Cazat, J.; Basset, J. M. *Science* **1997**, *276*, 99.
- (12) (a) Nozaki, C.; Lugmair, C. G.; Bell, A. T.; Tilley, T. D. *J. Am. Chem. Soc.* **2002**, *124*, 13194. (b) Stockenhuber, M.; Hudson, M. J.; Joyner, R. W. *J. Phys. Chem. B* **2000**, *104*, 3370.
- (13) (a) Johnson, B. F. G.; Raynor, S. A.; Shephard, D. S.; Maschmeyer, T.; Thomas, J. M.; Sankar, G.; Bromley, S. T.; Oldroyd, R. D.; Gladden, L. G.; Mantle, M. D. *Chem. Commun.* **1999**, 1167. (b) Raja, R.; Thomas, J. M.; Jones, M. D.; Johnson, B. F. G.; Vaughan, D. E. W. *J. Am. Chem. Soc.* **2003**, *125*, 14982.
- (14) (a) van't Blik, H. F. J.; van Zon, J. B. A. D.; Huizinga, T.; Vis, J. C.; Koningsberger, D. C.; Prins, R. J. *J. Am. Chem. Soc.* **1985**, *107*, 3139. (b) Ramaswamy, V.; Tripathi, B.; Srinivas, D.; Ramaswamy, A. V.; Cattaneo, R.; Prins, R. J. *Catal.* **2001**, *200*, 250. (c) Trouillet, L.; Toupance, T.; Villain, F.; Louis, C. *Phys. Chem. Chem. Phys.* **2000**, *2*, 2005. (d) Carriat, J. Y.; Che, M.; Kermarec, M.; Verdager, M.; Michalowicz, A. *J. Am. Chem. Soc.* **1998**, *120*, 2059. (e) Cheah, S.-F.; Brown, G. E.; Parks, G. A. *J. Colloid Interface Sci.* **1998**, *208*, 110. (f) Xia, K.; Bleam, W.; Helmke, P. A. *Geochim. Cosmochim. Acta* **1997**, *61*, 2211. (g) O'Day, P. A.; Chisholm-Brause, C. J.; Towle, S. N.; Parks, G. A.; Brown Jr. G. E. *Geochim. Cosmochim. Acta* **1996**, *60*, 2515. (h) Fitts, J. P.; Persson, P.; Brown, Jr. G. E.; Parks, G. A. *J. Colloid Interface Sci.* **1999**, *220*, 133.
- (15) Zhao, D.; Feng, J.; Huo, Q.; Melosh, N.; Fredrickson, G. H.; Chmelka, B. H.; Stucky, G. D. *Science* **1998**, *279*, 548.
- (16) Terry, K. W.; Lugmair, C. G.; Gantzel, P. K.; Tilley, T. D. *Chem. Mater.* **1996**, *8*, 274.
- (17) Tsuda, T.; Hashimoto, T.; Saegusa, T. *J. Am. Chem. Soc.* **1972**, *94*, 658.
- (18) Fudjald, K.; Drake, I. J.; Tilley, T. D.; Bell, A. T. *J. Am. Chem. Soc.* **2004**, *126*, 10864.
- (19) Brunauer, S.; Emmett, P. H.; Teller, E. *J. Am. Chem. Soc.* **1938**, *60*, 309.
- (20) Barrett, E. P.; Joyner, L. G.; Halenda, P. P. *J. Am. Chem. Soc.* **1951**, *73*, 373.
- (21) Fudjald, K. L.; Tilley, T. D. *J. Am. Chem. Soc.* **2001**, *123*, 10133.
- (22) The premonochromator slit was set larger than 1.0 mm for CuOSi/SBA (5.0) and CuO/Bu/SBA (3.5) defining a resolution greater than 2 eV for these samples. The XANES features of these samples were less resolved than desired. It is known that differences in resolution do not affect the EXAFS, because the EXAFS oscillates much more slowly than the energy width, except perhaps right near the edge.
- (23) Jentoft, R. E.; Deutsch, S. E.; Gates, B. C. *Rev. Sci. Instrum.* **1996**, *67*, 2111.
- (24) (a) Stern, E. A.; Kim, K. *Phys. Rev. B: Condens. Matter Mater. Phys.* **1981**, *23*, 378. (b) Koningsberger, D. C.; Prins, R. *X-ray Absorption*; Wiley: New York, 1988. (c) Koningsberger, D. C.; Mojet, B. L.; van Dorssen, G. E.; Ramaker, D. E. *Top. Catal.* **2000**, *10*, 143. (d) Teo, B. K. *EXAFS: Basic Principles and Data Analysis*; Springer: New York, 1986.
- (25) (a) Ressler, T. <http://www.winaxs.de>. (b) Ressler, T. *J. Phys. IV* **1997**, *7*, C2. (c) Ressler, T. *J. Synchrotron Radiat.* **1998**, *5*, 118.
- (26) Stern, E. A.; Newville, M.; Ravel, B.; Yacoby, Y.; Haskel, D. *Physica B* **1995**, *208/209*, 117.
- (27) (a) Newville, M. *J. Synchrotron Radiat.* **2001**, *8*, 322. (b) IFEFFIT manual; <http://cars9.uchicago.edu/ifeffit/>.
- (28) Newville, M.; Liviš, P.; Yacoby, Y.; Rehr, J. J.; Stern, E. A. *Phys. Rev. B: Condens. Matter Mater. Phys.* **1993**, *47*, 14126.
- (29) Bell, J. B. *Introductory Fourier Transform Spectroscopy*; Academic Press: New York, 1972.
- (30) (a) Ankudinov, A. L.; Rehr, J. J. *Phys. Rev. B: Condens. Matter Mater. Phys.* **1997**, *56*, R1712. (b) Ankudinov, A. L.; Boudin, C.; Rehr, J. J.; Sims, J.; Hung, H. *Phys. Rev. B: Condens. Matter Mater. Phys.* **2002**, *65*, 104107.
- (31) Atomic coordinates for copper metal, CuO, Cu<sub>2</sub>O, CuCl, and Cu were taken from the Atoms.inp Archive. This archive is a database of crystallographic data, ready to be converted to input files for FEFF, hosted by the Consortium for Advanced Radiation Sources (CARS); <http://cars9.uchicago.edu/~newville/adb/>.
- (32) Greiser, T.; Weiss, E. *Chem. Ber.* **1976**, *109*, 3142.
- (33) (a) Rehr, J. J.; Albers, R. C. *Rev. Mod. Phys.* **2000**, *72*, 621. (b) Manual for FEFF 8; <http://feff.phys.washington.edu/feff/>.
- (34) This statistical value is related to the standard definition of  $\chi^2$  but is normalized to the number of degrees of freedom in the fit. The details of this calculation have been described elsewhere. Newville, M.; Ravel, B.; Haskel, D.; Rehr, J. J.; Stern, E. A.; Yacoby, Y. *Physica B* **1995**, *208/209*, 154.
- (35) Tranquada, J. M.; Heald, S. M.; Moodenbaugh, A. R. *Phys. Rev. B: Condens. Matter Mater. Phys.* **1987**, *36*, 5263.
- (36) (a) Shulman, R. G.; Yafet, Y.; Eisenberger, P.; Blumberg, W. E. *Proc. Natl. Acad. Sci. U.S.A.* **1976**, *73*, 1384. (b) Hu, V. H.; Chan, S. I.; Brown, G. S. *Proc. Natl. Acad. Sci. U.S.A.* **1977**, *74*, 3821. (c) Nguyen, H. T.; Nakagawa, K. H.; Hedman, B.; Elliott, S. J.; Lidstrom, M. E.; Hodgson, K. O.; Chan, S. I. *J. Am. Chem. Soc.* **1996**, *118*, 12766. (d) Kau, L.; Spirak-Solomon, D. J.; Penner-Hahn, J. E.; Hodgson, K. O.; Solomon, E. I. *J. Am. Chem. Soc.* **1987**, *109*, 6433. (e) Dubois, J. L.; Mukherjee, P.; Stack, T. D. P.; Hedman, B.; Solomon, E. I.; Hodgson, K. O. *J. Am. Chem. Soc.* **2000**, *122*, 5775. (f) Prestipino, C.; Berlier, G.; Llabrés I Xamena, F. X.; Spoto, G.; Bordiga, S.; Zecchina, A.; Turnes Palomino, G.; Yamamoto, T.; Lamberti, C. *Chem. Phys. Lett.*, **2002**, *363*, 389.
- (37) (a) Choi, S. H.; Wood, B. R.; Ryder, J. A.; Bell, A. T. *J. Phys. Chem. B* **2003**, *107*, 11843. (b) Sayers, D. E.; Bunker, B. A. In *X-ray Absorption: Principles, Applications, Techniques of EXAFS, SEXAFS, and XANES*; Koningsberger, D. C., Prins, R., Eds.; John Wiley & Sons: New York, 1988; p 211. (c) Vaarkamp, M. *Catal. Today* **1998**, *39*, 271.
- (38) O'Day, P. A.; Rehr, J. J.; Zabinsky, S. I.; Brown, G. E., Jr. *J. Am. Chem. Soc.* **1994**, *116*, 2938.
- (39) Evans, H. T.; Mrose, M. E. *Am. Mineral.* **1977**, *62*, 491 (Crystallographic coordinates for shattuckite (Cu<sub>5</sub>(SiO<sub>3</sub>)<sub>4</sub>(OH)<sub>2</sub> and planchite (Cu<sub>8</sub>(Si<sub>4</sub>O<sub>11</sub>)<sub>2</sub>(OH)<sub>4</sub>·xH<sub>2</sub>O)).
- (40) Ribbe, P. H.; Gibbs, G. V.; Hamil, M. M. *Am. Mineral.* **1977**, *62*, 807 (Crystallographic coordinates for diopside (Ca<sub>2</sub>[Si<sub>2</sub>O<sub>6</sub>])).
- (41) Montano, P. A.; Shenoy, G. K.; Alp, E. E.; Schulze, W.; Urban, J. *Phys. Rev. Lett.* **1986**, *56*, 2076.
- (42) (a) Lopez, N.; Illas, F.; Pacchioni, G. *J. Phys. Chem. B* **1999**, *103*, 1712. (b) Lopez, N.; Illas, F.; Pacchioni, G. *J. Am. Chem. Soc.* **1999**, *121*, 813.
- (43) (a) *Nanomaterials: Synthesis, Properties and Applications*; Edelstein, A. S., Cammarata, R. C., Eds.; Institute of Physics Publishing: Bristol, 1998. (b) Boswell, F. W. C. *Proc. Phys. Soc. (London)* **1951**, *A64*, 465. (c) Vermaak, J. S.; Mays, C. W.; D., K.-W. *Surf. Sci.* **1968**, *12*, 128. (d) Woltersdorf, J.; Nepijko, A. S.; Pippel, E. *Surf. Sci.* **1981**, *106*, 64. (e) Heineman, K.; Poppa, H. *Surf. Sci.* **1985**, *156*, 265. (f) Teranishi, T.; Miyake, M. *Chem. Mater.* **1998**, *10*, 594 and references therein. (g) Goyhenex, C.; Henry, C. R.; Urban, J. *Philos. Mag. A* **1994**, *69*, 1073. (h) Lamber, R.; Weiten, S.; Jaeger, N. I. *Phys. Rev. B: Condens. Matter Mater. Phys.* **1995**, *51*, 10968. (i) Kaszkur, Z. *J. Appl. Crystallogr.* **2000**, *33*, 87.
- (44) (a) Frenkel, A. I. *J. Synchrotron Rad.* **1999**, *6*, 293. (b) Nashner, M. S.; Frenkel, A. I.; Somerville, D.; Hills, C. W.; Shapley, J. R.; Nuzzo, R. G. *J. Am. Chem. Soc.* **1998**, *120*, 8093. (c) Frenkel, A. I.; Hills, C. W.; Nuzzo, R. G. *J. Phys. Chem. B* **2001**, *105*, 12589. (d) Calvin, S.; Miller, M. M.; Goswami, R.; Cheng, S.-F.; Mulvaney, S. P.; Whitman, L. J.; Harris, V. G. *J. App. Phys.* **2003**, *94*, 778.
- (45) Cheah, S.; Brown, G. E., Jr.; Parks, G. A. *Am. Mineral.* **2000**, *85*, 118.
- (46) (a) Peri, J. B.; Hensley, A. L. *J. Phys. Chem.* **1968**, *72*, 2926. (b) Burwell, R. L. *CHEMTECH* **1974**, June, 371.
- (47) (a) Fung, S. C. *J. Catal.* **1990**, *122*, 202. (b) Fung, S. C. *Stud. Surf. Sci. Catal.* **2001**, *139*, 399. (c) Fung, S. C. *Catal. Today* **1999**, *53*, 325.